Correlated time variability of multicomponent high-velocity outflows in J162122.54+075808.4

P. Aromal,[1]★ R. Srianand[1]★ and P. Petitjean[2]★

[1]*IUCAA, Postbag 4, Ganeshkind, Pune 411007, India*
[2]*Institut d'Astrophysique de Paris, Sorbonne Universités and CNRS, 98 bis boulevard Arago, F-75014 Paris, France*

ABSTRACT

We present a detailed analysis of time variability of two distinct C IV broad absorption line (BAL) components seen in the spectrum of J162122.54+075808.4 ($z_{em} = 2.1394$) using observations from SDSS, NTT, and SALT taken at seven different epochs spanning about 15 yr. The blue-BAL component (with an ejection velocity, $v_e \sim 37\,500$ km s^{-1}) is an emerging absorption that shows equivalent width variations and kinematic shifts consistent with acceleration. The red-BAL component ($v_e \sim 15\,400$ km s^{-1}) is a three-component absorption. One of the components is emerging and subsequently disappearing. The two other components show kinematic shifts consistent with acceleration coupled with equivalent width variability. Interestingly, we find the kinematic shifts and equivalent width variability of the blue- and red-BAL components to be correlated. While the C IV emission-line flux varies by more than 17 per cent during our monitoring period, the available light curves (covering rest frame 1300–2300 Å) do not show more than a 0.1 mag variability in the continuum. This suggests that the variations in the ionizing flux are larger than that of the near-ultraviolet flux. However, the correlated variability seen between different BAL components cannot be explained solely by photoionization models without structural changes. In the framework of disc wind models, any changes in the radial profiles of density and/or velocity triggered either by disc instabilities or by changes in the ionizing radiation can explain our observations. High-resolution spectroscopic monitoring of J1621+0758 is important to understand the physical conditions of the absorbing gas and thereby to constrain the parameters of disc wind models.

Key words: galaxies: active – quasars: absorption lines – quasars: general – quasars: individual: J162122.54+075808.4.

1 INTRODUCTION

Strong outflows with velocities reaching up to few 10 000 km s^{-1} are seen in quasar spectra as blue-shifted broad absorption lines (BALs) with velocity widths of several 1000 km s^{-1}. Associated quasars are commonly known as 'BAL' quasars (Weymann et al. 1991). These powerful outflows can carry a significant amount of mechanical energy and momentum that can in principle contribute to active galactic nucleus (AGN) feedback mechanisms, regulating the central black hole growth and the host galaxy evolution (Ostriker et al. 2010; Kormendy & Ho 2013). They might interact with the inter-stellar medium of the host galaxies which can result in quenching or enhancement of star formation. If these outflows can escape the galactic potential wells, they can also contribute to the chemical enrichment of the intergalactic medium in the vicinity of galaxies.

The time variability of BAL profiles is a powerful tool for studying the origin and evolution of BAL outflows. Monitoring BAL variability over different time-scales can put tight constraints on the BAL lifetime, location of the outflow, etc., and provide significant insights on the origin and physical mechanisms driving the flow. The time variability of C IV, Si IV, and Mg II BAL profiles has been studied extensively in the literature. BAL variability includes extreme optical depth variations like emergence, disappearance, and kinematic shift

of BALs (Filiz Ak et al. 2013; McGraw et al. 2017; De Cicco et al. 2018; Rogerson et al. 2018; Vivek, Srianand & Dawson 2018). Possible reasons for these variations include: (i) fluctuations in quasar ionizing flux, (ii) changes in covering fraction of the outflow with respect to the central source, (iii) bulk motion of the outflow. It has been found that significant changes in the equivalent width and/or shape of the BAL trough occur typically on time-scales of few months to years in the quasar rest frame (see, for example, Filiz Ak et al. 2013; Vivek et al. 2014).

Among all outflows, ultra-fast AGN outflows (UFOs) are of great interest as they probe the inner regions of the central engine. Tombesi et al. (2010) defined UFOs as highly ionized absorbers detected mostly through Fe K shell absorption lines in X-rays at velocities $v_{outflow} \geq 10^4$ km s^{-1}. The high velocities and high ionization state of the absorbers (mainly H-like and He-like Fe) are usually attributed to their origin from within a few hundred gravitational radii from the central black hole where high-energy photons are produced. Ultraviolet (UV) absorptions from such BALs are commonly observed (Srianand & Petitjean 2001). They tend to show larger variability, emergence, and acceleration in their BAL profiles (Capellupo et al. 2011; Grier et al. 2016; Vivek et al. 2018). Recently, Rodríguez Hidalgo et al. (2020a) have studied a sample of extremely high-velocity outflows (EHVO; defined as absorption with outflow velocities between 0.1 and 0.2c). These outflows are detected in 0.6 per cent of quasars searched for C IV absorption. While Ly α associated with the C IV component is either not detected or weak,

★ E-mail: aromal@iucaa.in (PA); anand@iucaa.in (RS); ppetitje@iap.fr (PP)

~50 per cent of these BALs show associated N V absorption, and about 13 per cent show O VI absorption. These objects tend to have higher black hole mass and bolometric luminosities compared to the general population. Unfortunately, X-ray observations of these high-z EVHOs are not available which makes it difficult to establish any connection between them and X-ray detected UFOs.

Possible acceleration mechanisms through which outflows reach such high velocities are still debated. Photon scattering by free electrons alone is not sufficient for the absorbing gas to be accelerated to UFO (or EHVO) velocities. Radiative acceleration through UV line absorption has often been invoked (Arav & Li 1994; Murray et al. 1995; Proga, Stone & Kallman 2000) since observational pieces of evidence such as line-locking (Srianand 2000) or Ly α ghost (Arav 1996) strongly support line-driven BAL outflows. Another alternate mechanism is known as magnetic driving that can also explain highly ionized UFOs (de Kool & Begelman 1995). Even though these models are successful in explaining the observed BAL features, they all predict the outflows to be located very close to the central source at a distance of the order of 0.01–0.1 pc. If true, despite carrying large amounts of mechanical energy and momentum, they may have little influence on the large-scale star formation properties of the host galaxy.

The SDSS survey provides us with multi-epoch spectroscopic observations of BAL quasars allowing us to study BAL variability over the period the survey is performed. We have identified a sample of 31 BAL quasars showing large variability in the SDSS and conducted a spectroscopic monitoring at shorter time-scale using the South African Large Telescope (SALT). Here, we present a detailed analysis of an interesting BAL quasar, J162122.54+075808.4 (z_{em} = 2.1394), hereafter refer to as J1621+0758, from our sample. This quasar shows emergence of a BAL component with UFO (and EHVO) velocities followed by a kinematic shift in the BAL profile implying acceleration along our line of sight. In addition to the emerged component, an already existing BAL at comparatively lower velocities (while still satisfying the definition of UFOs) also shows high variability. Interestingly, the variability of these two distinct components are highly correlated. We also report time variability of C IV and Si IV emission line equivalent widths during our monitoring period. We find that the available light curves are consistent with no long-term brightening or fading of J1621+0758. *Thus, J1621+0758 is an interesting target to understand the origin and evolution of UFOs (or EHVOs) through variability studies. This forms the main motivation of this paper.*

The paper is organized as follows. In Section 2, we present the details of spectroscopic observations of J1621+0758 using SALT and ESO/NTT and data reduction. In Section 3, we provide the details of the C IV BAL components and quantify their rest equivalent width and kinematic variability. We probe the possible correlated variability in the C IV rest equivalent width and outflow velocities between different BAL components. In Section 4, we study the long-term rest UV continuum flux and colour variability of J1621+0758 using all the available spectra and photometric light curves. In Section 5, we discuss our results in the framework of simple photoionization models and simple disc wind model predictions. We summarize our main findings in Section 6.

2 OBSERVATIONS AND DATA REDUCTION

A C IV broad absorption with $z_{abs} \sim 1.9818$ is detected in the initial spectrum of J1621+0758 obtained for SDSS in the year 2005. A new C IV BAL at $z_{abs} \sim 1.7687$ emerged in another SDSS spectrum

taken in year 2012. This prompted us to undertake spectroscopic monitoring of J1621+0758 using the SALT (Buckley et al. 2005).

In the SDSS catalogue (Pâris et al. 2012), the quoted emission redshift of J1621+0758 is z_{em} = 2.134 49 ± 0.000 32. Hewett & Wild (2010) derive a systemic redshift of z_{em} = 2.139 449 ± 0.000 335 from the fit of the C III] emission. We use this latter value as the systemic redshift for all discussions in this paper. Note that given the high velocities of the BALs we observe here, the exact emission redshift has little influence on our study. Indeed, with respect to this systemic redshift the above identified two BAL components have ejection velocities of ~15 400 and 37 500 km s^{-1} based on the positions of the maximum C IV optical depths. We denote the two BAL components as 'red-' and 'blue-' BALs, respectively

Rodríguez Hidalgo et al. (2020b) found that, in a parent sample of 6760 quasars (please refer to section 2 of their paper for details) from Pâris et al. (2012), only ~ 14 per cent show C IV BALs according to the conventional definition (Weymann et al. 1991) and an even lesser fraction of ~0.6 per cent show extremely high-velocity outflow (EHVO) with velocities ranging from 30 000 to 60 000 km s^{-1}. J1621+0758 falls into this special type of BAL quasars due to the high ejection velocity of one of the C IV absorption components.

The log of SDSS, NTT, and SALT observations, details of the spectra, absorption lines, and reddening measurements are summarized in Table 1. New spectroscopic observations of J1621+0758 were carried out as part of our BAL quasar spectroscopic monitoring program with the SALT (Programme IDs: 2015-1-SCI-005, 2018-1-SCI-009, 2019-1-SCI-019, and 2020-1-SCI-011). We used the Robert Stobie Spectrograph (RSS; Burgh et al. 2003; Kobulnicky et al. 2003) in the long-slit mode using a slit 1.5 arcsec wide and the PG0900 grating (kept at a position angle, PA = 0.0). With GR angle = 14.75° and CAM angle = 29.5°, this setting provides a wavelength coverage of 4060–7120 Å excluding the 5065–5122 and 6115–6170 Å regions falling in the CCD gaps. The spectral resolution and average signal-to-noise ratio (S/N) obtained are summarized in columns 5 and 6 of Table 1. Our SALT spectra typically have a spectral resolution of $R \sim 985$ (roughly a factor of two smaller than that of SDSS) at central wavelength 5620 Å and S/N in the range 18–45 per pixel.

The raw CCD frames have been preliminary processed using the SALT data reduction pipeline (Crawford et al. 2010). We used then standard IRAF[1] procedures to reduce the resulting 2D spectra. Flat-field corrections and cosmic ray zapping were applied to all science frames. We extracted the one-dimensional quasar spectrum from the background subtracted 2D science frames from each epoch using the IRAF task 'Apall'. Wavelength calibration was performed using standard Argon lamp spectra. In addition, skylines from the wavelength calibrated spectrum were matched with the sky line atlas provided by SALT and, if needed, corrections were applied to increase wavelength accuracy. Similarly, flux calibration was performed using reference stars (G93-48 and LTT4364) observed close to our observing nights.

Prior to our SALT observations we also observed J1621+0758 using NTT as a backup target (for the ESO programme 093.A-0255; PI: R. Srianand) under overcast conditions, high airmass (~2) and good seeing (i.e. ~1 arcsec) conditions. We have used Grism GR#7 of EFOSC2 with a slit width of 1.5 arcsec. We obtained two exposures of 30 min each and the data were recorded with a 2 × 2 CCD binning.

---

[1]IRAF is distributed by the National Optical Astronomy Observatories, which are operated by the Association of Universities for Research in Astronomy, Inc., under cooperative agreement with the National Science Foundation.

Table 1. Log of observations and details of spectra obtained at different epochs.

Telescope used	Date [a] (D/M/Y)	(MJD)	Exposure time (s)	Spectral res. (km s^{-1})	S/N[b]	EW$^B_{1548}$[c] (Å)	EW$^R_{1548}$[d] (Å)	A_V[e]	p[f]	$g - r$[g]
SDSS	11-05-2005	53501	4200	150	19.41	–	2.70 ± 0.17	0.03	0.16 ± 0.01	....
SDSS	30-03-2012	56016	4200	150	28.69	3.66 ± 0.09	4.72 ± 0.12	0.17	0.59 ± 0.01	....
NTT	21-07-2014	56859	2×1800	650	7.11	5.11 ± 0.68	8.63 ± 0.79	....	....	....
SALT	08-06-2015	57181	2000	304	40.35	5.52 ± 0.08	6.99 ± 0.09	0.11	0.43 ± 0.01	....
SALT	07-05-2018	58245	2×1150	304	18.29	3.39 ± 0.19	5.46 ± 0.25	0.09	0.36 ± 0.01	0.22 ± 0.04
SALT	03-05-2019	58606	2×1150	304	26.91	2.69 ± 0.12	4.76 ± 0.15	0.07	0.28 ± 0.01	0.22 ± 0.04
SALT	21-05-2020	58991	2170	304	44.86	3.03 ± 0.07	4.01 ± 0.09	0.16	0.65 ± 0.01	0.27 ± 0.05

Notes. [a]Date of observations.
[b]Signal-to-noise ratio per pixel calculated over the wavelength range 5200–5500 Å for SDSS and SALT data and 4900–5180 Å for NTT data.
[c,d]Total C IV rest equivalent width of 'blue-' and 'red-BAL' components obtained by integrating over the absorption profile, respectively.
[e]Best-fitting parameter value of A_V as obtained from χ^2 minimization.
[f]Best-fitting parameter value of p in $C(\frac{\lambda}{\lambda_0})^p$, mimicking a change in the power-law spectrum relative to the template, as obtained from χ^2 minimization.
[g]$g - r$ colour obtained from the closest (i.e. within 1 d) available photometric measurements as explained in Section 4.2.

The data were reduced using standard IRAF procedures. As we do not have standard star observations, flux calibration was not performed. Also the available arc lamp spectrum does not have strong emission lines close to the blue-BAL component. Therefore, we correct the wavelength solution using nearby intervening absorption lines. The details of the NTT spectra are also summarized in Table 1.

We detect intervening Mg II absorption systems at $z_{abs} = 1.837\,39$ and $1.842\,01$ and C IV systems at $z_{abs} = 1.894\,83$, $2.005\,75$, and $2.046\,49$. Various narrow metal absorption lines from these systems are present in the same wavelength range as the 'red-' and 'blue-BAL' components. These lines give us strong constraints on any velocity shift in the C IV broad absorption as a function of time. We believe these are intervening absorbers as, (i) the ejection velocities are larger than 5000 km s^{-1}, (ii) we do not detect associated N V absorption, and (iii) C IV equivalent width does not show time variations between two SDSS epochs where the C IV doublet is resolved. In total, we have spectroscopic observations of J1621+0758 during seven epochs spread over 15 yr. We denote them by epoch-1, epoch-2, etc., in chronological order.

3 ANALYSIS OF SPECTRAL VARIABILITY

In this section, we present the observed properties of the two BAL components, their time evolution and correlated variabilities. We also study in detail the variability of the emission line profiles. For absorption line studies, we have normalized the spectra with the unabsorbed continuum determined by fitting low-order polynomials to the quasar emission. The normalized spectra around the C IV absorption are shown in Fig. 1. It is most likely that all absorptions we see are part of the same flow, for presentation purpose we consider 'blue-' and 'red-BAL' components separately in our discussion.

3.1 Kinematic and equivalent width variability of the red-BAL

As seen from the right-hand panels of Fig. 1, the C IV absorption profile of the red-BAL shows significant variability in terms of velocity spread, equivalent width, number of distinct absorption components, and kinematic shifts. To quantify these, we approximated the C IV absorption profile of the red-BAL component with multiple Gaussians (each velocity component will have a double Gaussian to take care of the C IV doublet absorption). These fits are also shown in Fig. 1 and corresponding fit parameters are summarized in Table 2. Column 3 of this table provides the velocity centroid of the individual Gaussian components. The difference in velocity centroid between

two subsequent epochs is used to measure the acceleration given in column 4. The Gaussian velocity widths quoted in column 5 of this table for individual components are consistent with them being mini-BALs. The equivalent widths quoted in column 6 is the sum of the C IV $\lambda 1548$ and C IV $\lambda 1550$ doublet lines and the errors are computed by fitting 1000 randomly generated spectra using the measured flux errors to randomize the flux in each pixel. The associated Si IV absorption is detected in component A during epoch-4. We were able to fit both C IV and Si IV with a consistent set of Gaussian parameters (i.e. width and centroid) during this epoch. The rest equivalent widths (or 3σ upper limits) of C IV and Si IV are provided in columns 6 and 7, respectively.

During the first SDSS epoch (epoch-1), we identify the red-BAL as a single shallow and broad [full width at half-maximum (FWHM) ~ 3050 km s^{-1}] absorption centred around outflow velocity of 15 000 km s^{-1} and with a C IV equivalent width of 2.50 ± 0.29 Å. We do not detect any other associated absorption, neither Si IV nor Al III. This epoch spectrum does not cover the expected wavelength range of N V and Lyα absorptions.

During epoch-2, the C IV BAL becomes stronger, the velocity range covered by the absorption has increased (i.e. ~ 5000 km s^{-1}) and the absorption profile also splits into two distinct components (separated by 2532.0 ± 210.8 km s^{-1}) each having similar C IV equivalent widths (i.e. 2.14 ± 0.32 and 2.24 ± 0.32 Å, respectively; see Table 2). It is also evident that C IV absorption profile for both the components is deeper than what is seen in the first epoch spectrum. We denote these two components as A and B in Fig. 1. The Si IV absorption from these components is not clearly detected at this epoch. The SDSS spectrum obtained during this epoch also covers the expected wavelength range of Lyα and N V absorption from the red-BAL. We do not find any strong absorption line at the expected position of H I Lyα absorption. However, we cannot rule out a possible weak absorption feature. We fit two Gaussians corresponding to A and B components of the red-BAL and derive upper limits on the Lyα equivalent widths to be 1.80 and 1.10 Å, respectively. If we assume the absorption to be on the linear part of the curve of growth, these limiting equivalent widths correspond to H I column density of $N(\text{H\,I}) \leq 1.7 \times 10^{15}$ cm^{-2} and $N(\text{H\,I}) \leq 1.1 \times 10^{15}$ cm^{-2} for A and B, respectively. The actual limiting column densities can be higher if the absorbing gas does not cover the background source completely.

In the spectra obtained using NTT (epoch-3) the C IV absorption, in addition to showing A and B components albeit with enhanced absorption strength, also shows a newly emerging strong component
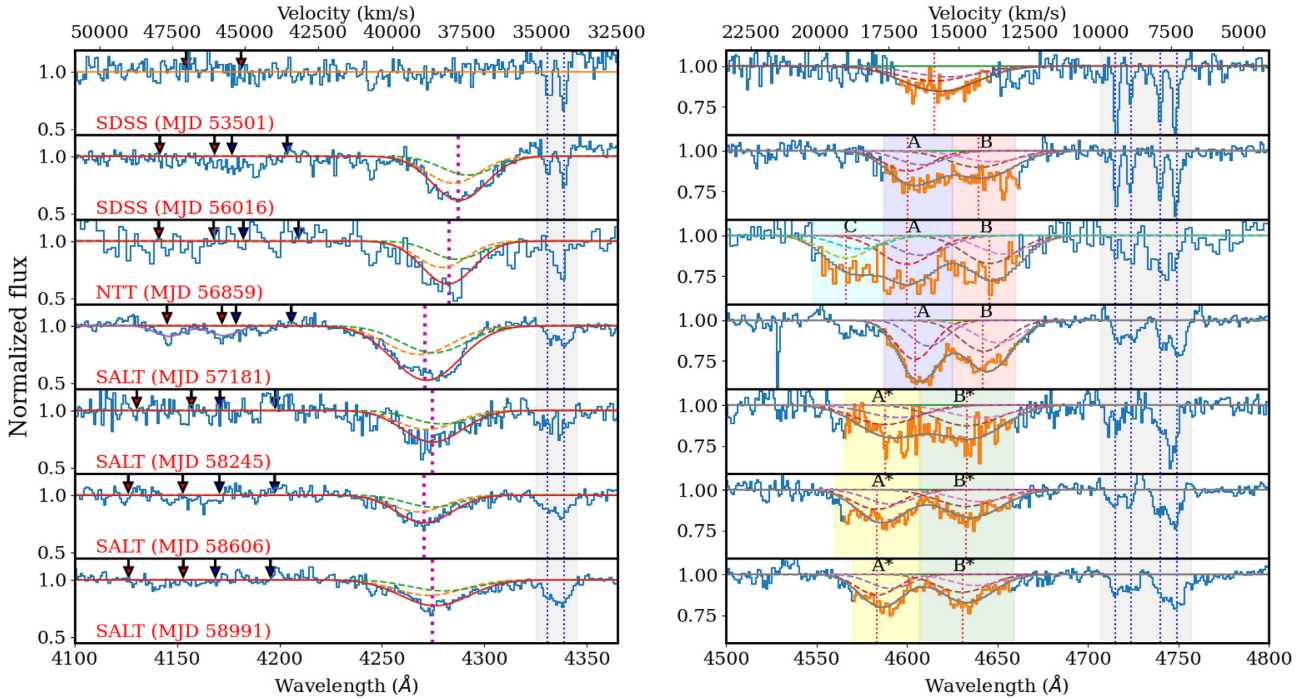
Figure 1. Normalized spectra (using lower order polynomials) showing the time evolution of 'blue' (left-hand panels) and 'red' (right-hand panels) C IV BALs. The relative velocity scale with respect to the systemic redshift of J1621+0758 (i.e. $z_{em} = 2.13945$) is given at the top. The absorption profiles are fitted with Gaussian components. The best fits are overplotted as red and grey solid lines in the left-hand and right-hand panels, respectively. In the right-hand panel, the filled regions marked with A, B, and C correspond to the regions where components A, B, and C of the red-BAL are located. The dashed lines in the figure correspond to the centres of individual Gaussian components contributing to the best fit (representing the C IV doublet lines for each BAL component). Intervening absorption lines are marked by blue dotted vertical lines inside the grey shaded regions. Black vertical arrows in the left-hand panels indicate the expected positions of the Si IV absorption associated with the C IV components identified in the red-BAL shown in the corresponding right-hand panels.

at $\sim$18 500 km s^{-1} (denoted as component C). This new component has a velocity separation of 2156 ± 239 km s^{-1} with respect to component A which is very close to the Si IV doublet splitting of 1925 km s^{-1}. High-resolution spectra would have been important to confirm such a velocity coincidence and support the line driven acceleration. This absorption is clearly seen in both the spectra obtained with NTT with a C IV rest equivalent width of 1.95 ± 0.33 Å. As before we do not detect Si IV absorption associated with any of these three C IV components in our spectrum at this epoch. Our NTT spectrum also covers Ly α and N V regions but we do not detect any significant absorption at the expected positions. *Our observation constrains the emerging time-scale for component 'C' to ≤ 268.5 d in the quasar rest frame.*

In the spectra taken during our first SALT epoch (epoch-4) component C, which was found to be emerging in the previous epoch, has become very weak [with a 3σ upper limit of $W(\text{C IV}) \leq 0.38$ Å]. Thus, the overall time-scale over which this component emerged and subsequently disappeared along our line of sight is ≤ 424.4 d in the quasar frame. This time-scale is within the smallest observed so far (Filiz Ak et al. 2012; McGraw et al. 2017; De Cicco et al. 2018). Components A and B are seen nearly at the same redshifts as in epoch-3 and their equivalent widths reach their maximum values (i.e. 3.29 ± 0.04 and 3.32 ± 0.06 Å respectively for A and B) (see Table 2). The optical depth variations are non-uniform throughout the BAL profile component A showing larger absorption optical depth changes compared to B (see Fig. 1). Interestingly, we observe the resolved Si IV absorption associated with component A (see the absorptions at the location of the first two arrows from the left in the corresponding left-hand panel for epoch-4 of Fig. 1). However,

we do not detect Si IV from component B. Unfortunately during this epoch our SALT spectrum does not cover the Ly α and N V absorption wavelength range.

In the next SALT epoch (epoch-5), the BAL becomes weaker with significant (non-uniform) changes in the absorption profile, indicating a possible kinematic shift. We note that the wavelength calibration is ascertained by the presence of intervening absorption lines at the same position in all spectra. These intervening absorption are shown with vertical dotted lines in grey shaded regions of Fig. 1. The absorption lines seen around 4720 Å are C IV doublets from the $z_{abs} = 2.04649$ system. Lines seen around 4750 Å are Al II absorption from the Mg II systems at $z_{abs} = 1.83739$ and $z_{abs} = 1.84201$. The Si II absorption from the same Mg II systems (around 4340 Å) are shown in the left-hand panel. We also confirm the wavelength solutions using the wavelength of the sky lines.

The C IV absorption profile at this epoch is also well fitted with two Gaussian components. We call these components as 'A*' and 'B*'. At the same time, the Si IV absorption associated with component A at epoch-4 has disappeared. The variations in the profile seen at this epoch with respect to the previous epochs are consistent with two possibilities (i) the C IV components A and B have accelerated (with associated variations in C IV optical depth) or (ii) the components A and B disappeared along our line of sight and new components A* and B* have emerged close to (albeit at slightly higher velocities) compared to A and B. The presence of two components with similar velocity separation favours the first possibility. However the optical depth change and the non-detection of Si IV absorption will be inconsistent with simple acceleration without profile changes discussed in the literature (Grier et al. 2016).

Table 2. Parameter values obtained from Gaussian fits of the BAL components.

BAL component	Epoch[a]	Velocity centroid (v_c)[b] (km s^{-1})	Acceleration (cm s^{-2})	Velocity width[c] (km s^{-1})	EW (C IV)[d] (Å)	EW (Si IV)[e] (Å)
	1	–	–	–	–	–
	2	16 478 ± 159	–	787 ± 77	2.14 ± 0.31	≤0.30
	3	16 588 ± 150	+0.47 ± 0.94	789 ± 60	3.35 ± 0.53	≤1.83
Red-BAL (A)	4	16 211 ± 60	− 4.25 ± 1.82	669 ± 24	3.29 ± 0.04	2.04 ± 0.09
	5	17 257 ± 199	+3.57 ± 0.71	1165 ± 624	2.70 ± 1.33	≤0.71
	6	17 574 ± 101	+3.19 ± 2.25	810 ± 84	2.18 ± 0.18	≤0.38
	7	17 571 ± 59	− 0.03 ± 1.11	693 ± 31	1.93 ± 0.07	≤0.21
	1	–	–	–	–	–
	2	13 946 ± 291	–	1005 ± 154	2.24 ± 0.32	≤0.33
	3	13 653 ± 175	− 1.26 ± 1.46	936 ± 135	2.52 ± 0.55	≤1.92
Red-BAL (B)	4	13 792 ± 40	+1.57 ± 2.02	781 ± 17	3.32 ± 0.06	≤0.35
	5	14 330 ± 185	+1.83 ± 0.64	1328 ± 488	3.19 ± 1.20	≤0.68
	6	14 386 ± 101	+0.57 ± 2.11	987 ± 92	2.22 ± 0.16	≤0.40
	7	14 519 ± 55	+1.25 ± 1.08	881 ± 62	2.02 ± 0.10	≤0.23
Red-BAL (C)	3	18 765 ± 177	–	799 ± 59	1.95 ± 0.33	–
	1	–	–	–	–	–
	2	37 592 ± 39	–	783 ± 21	4.04 ± 0.09	2.09 ± 0.17
	3	37 951 ± 320	+1.54 ± 1.39	807 ± 254	4.36 ± 1.45	0.95 ± 0.09
Blue-BAL	4	38 735 ± 17	+8.84 ± 3.62	991 ± 6	6.26 ± 0.03	–
	5	38 475 ± 90	− 0.88 ± 0.31	865 ± 93	3.22 ± 0.23	–
	6	38 769 ± 63	+2.95 ± 1.10	801 ± 63	2.59 ± 0.14	–
	7	38 406 ± 52	− 3.42 ± 0.76	994 ± 52	2.99 ± 0.11	–

Notes. [a]Spectroscopic observations in chronological order in time.
[b]Centroid of the Gaussian fits to the BAL components as explained in Section 3.1.
[c]One sigma width of the Gaussian fits to the BAL components.
[d]Equivalent width of C IV as calculated from the Gaussian fits.
[e]Equivalent width of Si IV as calculated from the Gaussian fits.

While we will consider the above two possibilities, for simplicity we quote these two components as A and B from now on.

During epoch-6 (i.e. MJD 58606), the two C IV absorption components A and B are well defined and there is a slight reduction in the C IV equivalent width with a possible kinematic shift (see Table 2). During this epoch, we do not detect any Si IV absorption. During epoch-7 (i.e. MJD 58991) C IV rest equivalent widths of A and B have further reduced without any additional kinematic shift.

It is also clear, from the 3σ upper limits on Si IV equivalent widths for component A, that not only the C IV equivalent width has changed but the ratio of Si IV to C IV equivalent widths has also changed with time (see Table 2).

3.2 Emergence, kinematic, and equivalent width variations of the blue-BAL

Emergence of the blue-BAL, located on the blue side of the Si IV emission line, is apparent in the epoch-2 SDSS spectrum with an outflow velocity of $\sim$37 000 km s^{-1}. The emergence time-scale of this component is $\leq$802 d in the quasar's rest frame. We also detect the Si IV doublet associated with this C IV absorption on top of the quasar Ly α + N V emission line. These absorption lines are well fitted with a single Gaussian component (see Figs 1 and 2). The Gaussian parameters for both C IV and Si IV absorptions are summarized in Table 2. We also detect an absorption at the location of Al III (see Fig. 2) with a rest equivalent width of 0.93 ± 0.10 Å.

In the epoch-3 spectrum obtained with NTT, we observe a shift in the C IV absorption feature without appreciable change in its rest equivalent width. This possible acceleration signature is illustrated by the Gaussian fits to the C IV and Si IV absorptions shown in
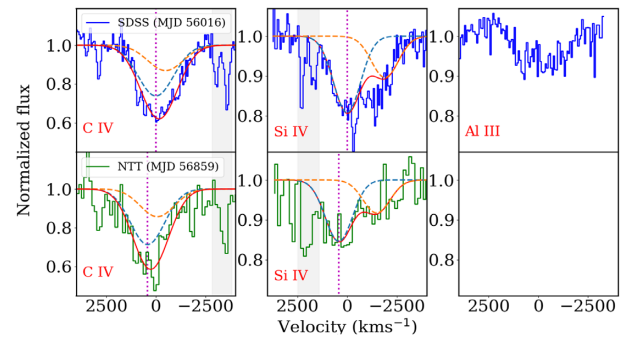

Figure 2. Gaussian fits to the C IV and Si IV absorption from the blue-BAL component (red solid lines) seen in spectra obtained with SDSS (MJD 56016; top panel) and NTT (MJD 56859; bottom panel) epochs. The dashed lines in the figure correspond to the individual Gaussian components contributing to the best fit (representing the C IV and Si IV doublet lines for each BAL component). Vertical dotted lines show the velocity centroid of the Gaussian component corresponding to the blue member of the C IV (in the left-hand panel) and Si IV (in the centre panel) doublet lines with respect to the absorption redshift $z_{abs} = 1.7688$ (measured using optical depth weighted centroid). The Al III absorption detected during epoch-2 is shown in the top right panel.

Fig. 2 showing that the kinematical shifts are consistent for the C IV and Si IV profiles. The acceleration inferred from the Gaussian centroid of the C IV absorption (see Table 2) is not statistically significant however due to poor SNR of our NTT data. Unlike the C IV absorption, the Si IV absorption shows approximately a factor of two reduction in the rest equivalent width.
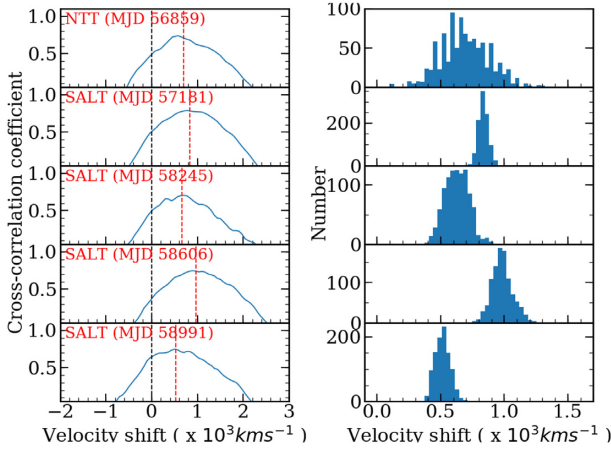
Figure 3. *Left-hand panels:* CCF for the C IV blue-BAL component obtained at different epochs with respect to the C IV profile observed in epoch-2. The centroid shift of the BAL profile is shown by the red dashed line and the zero velocity shift is shown by the black dashed line. *Right-hand panel:* Corresponding CCCDs from Monte Carlo simulations.

As for the red-BAL, the C IV equivalent width of the blue-BAL reaches its maximum in the epoch-4 SALT spectrum (on MJD 57181). From Fig. 1, it is clear that the noticed change in the C IV absorption profile is consistent with acceleration. If we consider the Gaussian centroids obtained from epoch-3 and epoch-4 spectra, we get an acceleration of $+8.84 \pm 3.61$ cm s^{-2} (significant at the 2.4σ level) Instead, if we consider epoch-2 and epoch-4 the inferred acceleration is 3.57 ± 0.08 cm s^{-2}. This is one of the largest accelerations inferred among BAL quasars (see fig. 6 of Grier et al. 2016). Our SALT spectra of this epoch and subsequent epochs do not cover the Si IV region.

From Fig. 1 (also see Table 2), we find that for the next three epochs the strength of the C IV absorption has reduced as in the case of the red-BAL components. We also notice the changes in the centroid of the Gaussian components used to fit the C IV absorption. However, these shifts (seen after the epoch-4) are not monotonous and their significance is typically at the 2–3σ level (see Table 2).

The kinematic shifts are usually quantified using cross-correlation analysis (see, for example, Grier et al. 2016; Joshi et al. 2019). We thus calculate the cross-correlation between the BAL profile in the epoch-2 spectrum with those obtained at subsequent epochs. We estimate the shift in wavelength using the location of the peak in the cross-correlation coefficient (r_{peak}) estimated using only points around the peak with values greater than $0.8r_{\mathrm{peak}}$. Taking into account measurement uncertainties, we randomize the flux in each pixels of both spectra and generate 1000 realizations to measure the cross-correlation function (CCF) and in each case the corresponding peak and centroid. The final velocity shift is the median of the cross-correlation centroid distribution (CCCD) and the 1σ uncertainty is the central interval encompassing 68 per cent of CCCD. The measured CCFs for different epochs are summarized in Fig. 3 and Table 3.

It is clear from this figure that compared to the epoch-2 spectrum the blue-BAL component observed in subsequent epochs shows clear sign of increase in the ejection velocity by $\sim$530 to $\sim$975 km s^{-1}. The measured acceleration between different epochs varies from 0.64 to 2.81 cm s^{-2} (see Table 3). These values are inconsistent with a nearly constant velocity one expects from simple disc wind models in late stages of the flow. Note the BAL quasars showing acceleration signatures often tend to show such behaviour whenever more than two epoch observations are available (Grier et al. 2016; Joshi et al.

Table 3. Results of cross-correlation analysis of the 'blue' BAL.

Epochs	Velocity shift (km s^{-1})	Acceleration (cm s^{-2})
2,3	654^{+194}_{-213}	$2.81^{+0.83}_{-0.91}$
2,4	837^{+27}_{-43}	$2.61^{+0.08}_{-0.13}$
2,5	639^{+95}_{-106}	$1.04^{+0.15}_{-0.17}$
2,6	974^{+81}_{-80}	$1.36^{+0.11}_{-0.11}$
2,7	530^{+33}_{-78}	$0.64^{+0.04}_{-0.09}$

2019). The blue-BAL that is seen as a single component in our low-resolution spectrum may have a multiple absorbing component structure. Any change (either individual optical depths or velocity centroids) in these components can lead to small centroid shifts in the overall absorption. While this cannot explain the large shifts seen in the earlier epochs, it could contribute to smaller shifts we see in the later epochs. The probability that the profile shapes between two epochs are identical after applying appropriate kinematic shifts as given in Table 3 is nearly zero for all the epochs considered in the cross-correlation analysis which is consistent with the appreciable profile variability we observe (Fig. 1). This suggests that the blue-BAL in addition to showing appreciable velocity shift also has strong optical depth variability. Thus, the variability found is inconsistent with a single absorbing gas accelerating along our line of sight without any change in the strength of the absorption it produces.

3.3 Is there a correlated variability?

In this section, we investigate the possible correlation between the variations (both in equivalent width and kinematic shift) of the blue- and red-BAL C IV components. In the top panel of Fig. 4, we plot the C IV equivalent widths (total as well as measured in individual Gaussian components A and B) as a function of time. The measured rest equivalent widths of C IV and Si IV at different epochs are also summarized in Table 2. It is clear from this figure that the total C IV equivalent width of the red-BAL increases during the first three epochs and then shows a steady decline afterwards. Interestingly, individual C IV equivalent widths of components A and B of the red-BAL show similar trend. As can be seen from Table 2 and Fig. 4, the C IV equivalent widths of A and B are consistent with one another within errors. However, the overall profile shape does not remain constant during various epochs (see Fig. 1). Both these components reach their maximum C IV equivalent width during epoch-4. It is also evident from the top panel of Fig. 4 that the C IV equivalent width of the blue-BAL follows the trend of the red-BAL. Thus, there appears to be a correlation between the blue- and red-BAL in the time evolution of the C IV equivalent width.

In the bottom panels of Fig. 4, we plot the ejection velocity of the red-BAL components A and B as a function of time. It is evident that both components A and B have blue-shifted between epoch-4 and epoch-5. However, the amount of shift is not the same for both components (i.e. 1045 ± 208 and 537 ± 189 km s^{-1} for A and B respectively based on the Gaussian centroids). This has led to significant increase in the velocity separation between the two components. This also implies that the acceleration (i.e. either velocity change or directional change) is not the same for both the components. After epoch-5, there is no significant change in the ejection velocity of the components A and B while their equivalent widths have shown a steadily declining trend. It is also clear from Fig. 4 (and the discussions presented in the previous section) that
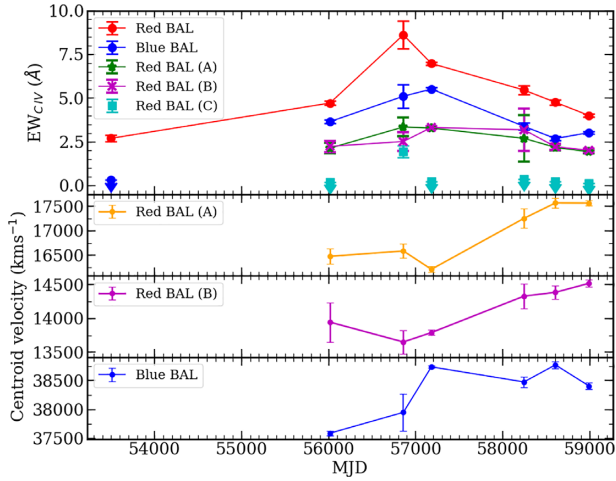
Figure 4. *Top panel*: C IV rest equivalent widths of different absorption components as a function of time. In the case of red-BAL, we plot the total equivalent width measured from the whole absorption as well as equivalent widths of individual Gaussian components (A, B, and C) given in Table 2. The downward arrows are 3σ upper limits when the absorption line is not clearly detected. *Bottom three panels*: Velocity centroid (third column in Table 2) of different C IV absorption components as a function of time.

blue-BAL has gone through an accelerated phase between epoch-2 and epoch-4. However, the maximum velocity for the blue-BAL component is achieved much earlier than that for red-BAL components. The maximum delay for red-BAL to reach its maximum velocity is ∼338 d in the quasar rest frame.

It seems there is some correlation between the variability of the red and blue-BALs. If ionization changes are involved in these

variabilities we should observe some variability of the emission line flux. We explore this in the following section.

3.4 Broad emission line variability

In this section, we study the variability of the broad emission lines. As we do not have accurate flux calibration (due to unknown slit losses) for our SALT spectrum first, we look at the C IV line equivalent width variations. For this, we normalize all the spectra (excluding the one obtained with NTT) around the C IV emission line using the continuum flux measured over the rest wavelength range 1585–1615 Å. The normalized C IV emission profile for different epochs are compared with that from epoch-1 in the bottom panel of Fig. 5. Similar plots for Si IV and Mg II are shown in the middle and top panels of this figure, respectively. The wavelength range of Si IV emission is severely contaminated by intervening absorption and the C IV absorption from the blue-BAL. Therefore, the normalization is not perfect in the case of the Si IV line. The Mg II emission line region is covered only in the SDSS spectra. In Table 4, we summarize the emission line equivalent widths measured for the blue (i.e. +500 to +6350 km s^{-1} with respect to the systemic redshift) and red (i.e. −6800 to +500 km s^{-1} with respect to the systemic redshift) side of the C IV emission peak. The chosen regions are of unequal width because we avoid the spectral range contaminated by intervening absorption (shaded regions in Fig. 5).

It is apparent from Fig. 5 and Table 4 that the C IV emission profile is asymmetric and skewed (i.e. more flux) towards the blue (i.e. low wavelength) side. Such asymmetric profiles are usually attributed to the presence of disc winds in the BLR (see, for example, Richards et al. 2011). This is the main reason for us to consider the red and blue part of C IV emission separately. The Mg II profile is contaminated by sky subtraction residuals. However, we do see a slight asymmetry of
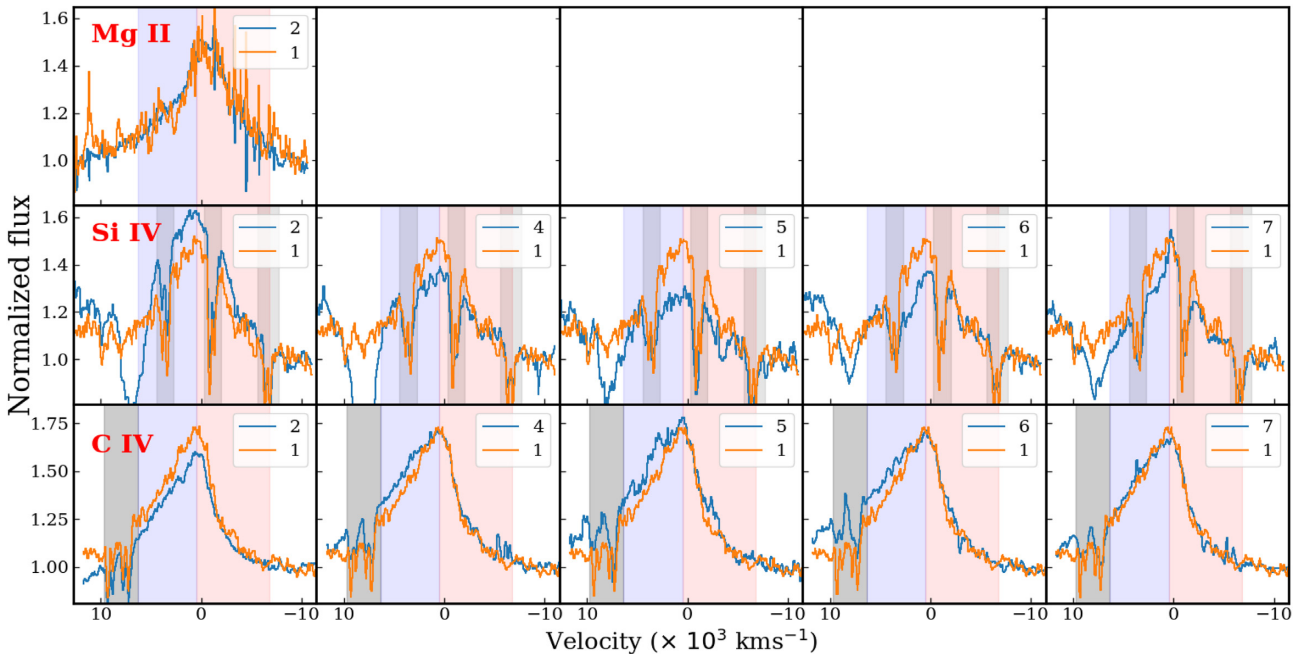

Figure 5. Comparison of emission profiles of C IV (bottom), Si IV (middle), and Mg II (top) observed at different epochs with the corresponding profiles obtained during epoch-1. All spectra are normalized to the median flux measured over a common rest-frame wavelength range. Spectral ranges affected by intervening absorption lines are marked with grey shaded regions. Red and blue part of the C IV emission lines are indicated with red and blue shaded regions. The figure illustrates the blue asymmetry of the C IV emission, the time variability of the profile and the fact that C IV and Si IV equivalent widths vary in the opposite direction. The velocity scale is defined with respect to the systemic redshift (i.e. $z = 2.13945$).

Table 4. Broad emission line variability.

Ion	Epoch	EW (blue) [a] (Å)	EW (red) [b] (Å)	$\frac{EW(blue)}{EW(red)}$
C IV	1	13.72 ± 0.19	8.83 ± 0.21	1.55 ± 0.04
	2	10.86 ± 0.13	7.19 ± 0.14	1.51 ± 0.03
	4	15.71 ± 0.10	9.69 ± 0.10	1.62 ± 0.02
	5	16.62 ± 0.22	10.07 ± 0.22	1.65 ± 0.04
	6	15.64 ± 0.14	9.36 ± 0.14	1.67 ± 0.03
	7	14.12 ± 0.08	8.82 ± 0.09	1.60 ± 0.02
Si IV	1	4.09 ± 0.13	2.43 ± 0.15	1.68 ± 0.12
	2	5.49 ± 0.10	3.73 ± 0.11	1.47 ± 0.05
	4	3.04 ± 0.06	2.19 ± 0.08	1.39 ± 0.07
	5	2.27 ± 0.14	1.16 ± 0.18	1.96 ± 0.33
	6	2.40 ± 0.09	2.36 ± 0.11	1.02 ± 0.06
	7	3.11 ± 0.06	1.94 ± 0.07	1.60 ± 0.10
Mg II	1	11.00 ± 0.63	20.38 ± 0.92	0.54 ± 0.04
	2	11.99 ± 0.32	18.06 ± 0.46	0.66 ± 0.02

Notes. [a]Equivalent width calculated for the velocity range 500–6350 km s^{-1} blueward of the systemic redshift for C IV and Mg II and 500–2600 km s^{-1} for Si IV.
[b]Equivalent width calculated for the velocity range 500 to −6800 km s^{-1} redward of the systemic redshift for C IV and Mg II and −2100 to −5500 km s^{-1} for Si IV.

the Mg II profile in Fig. 5. Moreover, when we use the same velocity range as that of C IV we do see the blue side having less flux compared to the red side.

From Fig. 5, we can see an initial decline, then an increase followed by a decreasing trend for the C IV equivalent width. The Si IV equivalent width seems to follow the opposite trend. It is also evident from Table 4 that both red and blue part of the C IV equivalent width show similar trend with variation in the blue part being larger. This is also reflected in the fact that the equivalent width ratio of blue and red parts (last column in Table 4) follows the trend with time seen in the C IV rest equivalent width. From the top panel in Fig. 5, we can see no clear variation for the Mg II profile between the first two SDSS epochs.

The emission line equivalent width variations can be driven by line and/or continuum variations. To quantify the flux variations, we first consider the spectra from first two epochs (i.e. SDSS spectra). In the top panel of Fig. 6, we show the difference between the two spectra as a function of wavelength. While calculating the difference spectrum we applied the correction to the BOSS spectrum as suggested by Guo & Gu (2016, using their equation 1). In this plot, we also mark the regions affected by emission and absorption. It is evident that the continuum shape has changed with more variations in the blue. We fit this difference spectrum with a third-order polynomial. By integrating the residual spectrum (after subtracting the fit) over the shaded region marked as C IV in Fig. 6, we estimate the reduction in the C IV flux to be $(4.82 \pm 0.69) \times 10^{-16}$ erg s^{-1} cm^{-2} between epoch-1 and epoch-2. This corresponds to a C IV line flux variation by ∼11 per cent between epoch-1 and epoch-2. We also find that the Si IV line flux has reduced by $(1.59 \pm 0.31) \times 10^{-16}$ erg s^{-1} cm^{-2} between epoch-1 and epoch-2. Therefore, the increase in Si IV equivalent width we note in Table 4 is dominated by the change in the continuum flux around the Si IV emission.

We have access to *g*- and *r*-band photometric measurements on the nights of last three SALT observations (see Fig. 9). Using this, we estimate the slit loss and obtain the absolute flux scale for these epochs. The *g* and *r* magnitudes have error of ∼0.03 mag. The difference of the spectra obtained during the last two SALT epochs (6 and 7) after correcting flux levels is shown in the
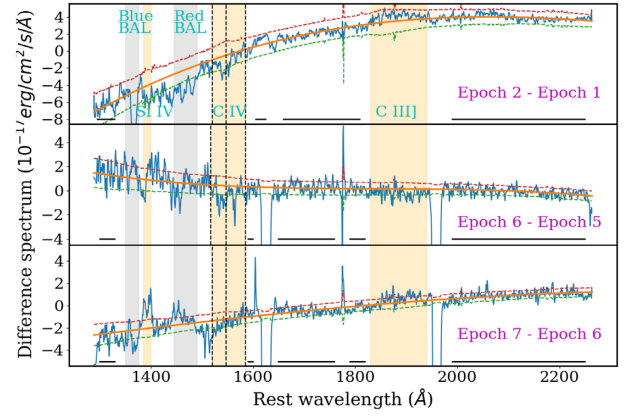
Figure 6. Difference of the J1621+0758 spectra observed at epoch-1 and 2 (top), epoch-5 and 6 (middle), and epoch-6 and 7 (bottom). The smooth third-order polynomial fit and associated 1σ flux errors are shown as solid and dotted curves, respectively. The regions used for the polynomial fit are shown by the horizontal black lines. The yellow and grey shaded regions show the wavelength range affected by emission and absorption lines.

bottom panel of Fig. 6. The C IV line flux has decreased between epoch-6 and epoch-7 by $(1.59 \pm 0.28) \times 10^{-16}$ erg s^{-1} cm^{-2}. This corresponds to a C IV line flux variation by 4 per cent. Given the flux uncertainties, this may not be a significant change. In the same way, we find that the C IV flux has been reduced between epoch-5 and 6 by $(5.03 \pm 0.30) \times 10^{-16}$ erg s^{-1} cm^{-2} (see the middle panel in Fig. 6). This is ∼13 per cent change in the C IV line flux. Thus during the last three spectroscopic epochs (where we have photometry to get absolute flux scales) we see the C IV emission line flux continuously decreasing by ∼17 per cent. Unfortunately we do not have photometric measurements during epoch-4 when the C IV equivalent width was maximum.

In low-*z* AGNs C IV is known to show a positive response to the continuum variations with some time-delay. Also C IV and Si IV tend to show similar responses (see De Rosa et al. 2015). In these AGNs, typical continuum variations are of the order of 20 per cent when emission lines variations are less. Our finding would imply large ionizing flux variations, as the BLR size of J1621+0758 is expected to be much larger than that of low-*z* low-luminosity AGNs. Such variations in the ionizing flux could also help us understand the origin of the absorption line variability.

4 CONTINUUM VARIABILITY

In this section, we focus on the continuum (i.e. flux as well as colour) variability of J1621+0758. For this purpose, we will use continuum fits to the observed spectra as well as photometric light curves.

4.1 Optical continuum and colour variations

We quantify the variability in the spectral shape by fitting the observed flux-calibrated spectra with a quasar template obtained from the SDSS spectra of 186 non-BAL quasars at $2.0 < z_{em} < 2.25$ having *r*- and *i*-band magnitudes within 0.2 mag of J1621+0758 magnitudes measured during the SDSS photometric survey. Any difference found between individual spectra and the template will be ascribed to dust-extinction or to the particular slope of the quasar continuum.

We reddened the composite spectrum using different [Large Magellanic Cloud, Small Magellanic Cloud (SMC), and Milky Way] extinction curves given in Gordon et al. (2003) and the method
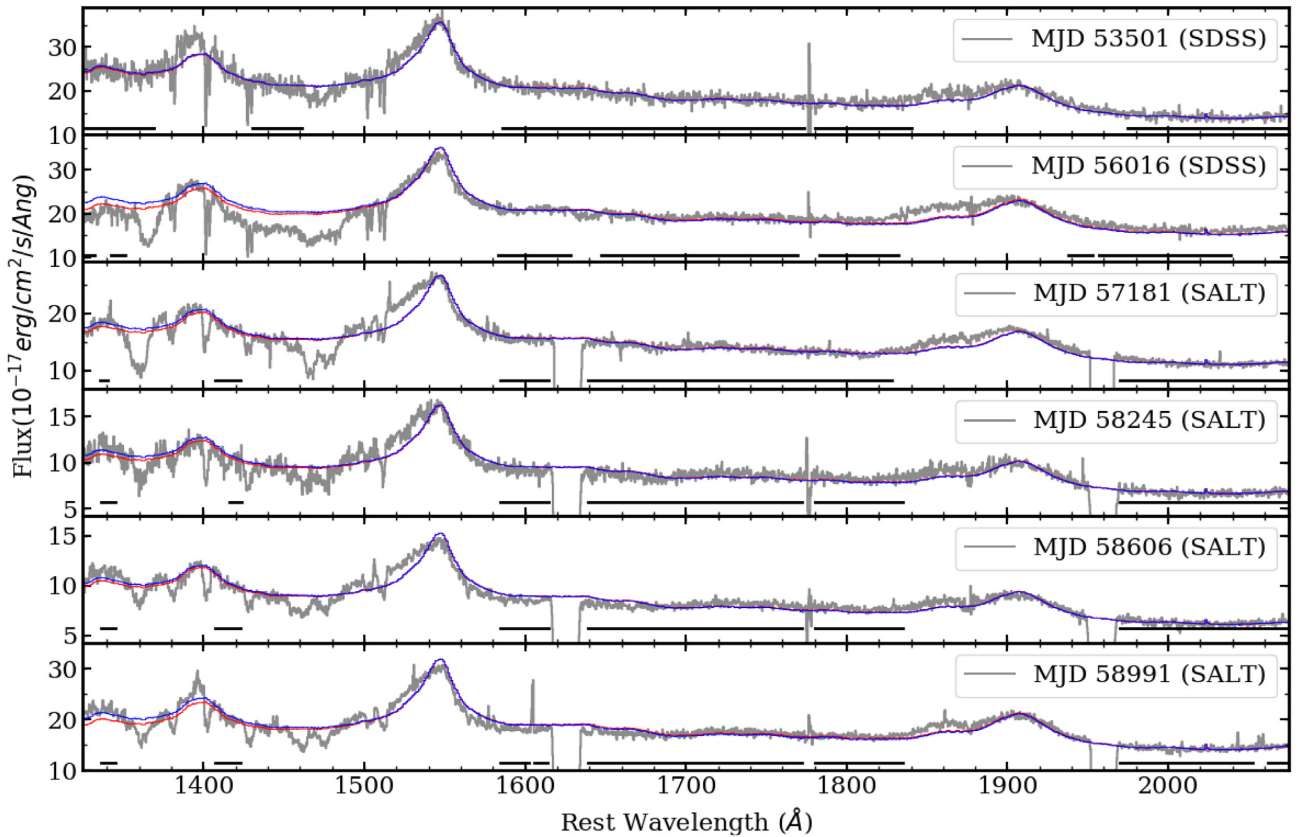
Figure 7. Observed spectra of J1621+0758 at different epochs. The spectrum obtained with NTT at epoch-3 is not shown as it was not possible to flux calibrate that spectrum. Wavelengths are given in the rest frame of the quasar at $z_{em} = 2.139\,45$. The red and blue curves are the results of the fit to the observations by a quasar template attenuated by dust or tilted by a power law, respectively, as discussed in Section 4. As expected, the two corrections are degenerated. The black horizontal lines mark the regions devoid of any absorption or emission lines which are used during the continuum fitting. Spectral gaps seen in the SALT spectra around $\lambda \sim 1630$ and $1960\,\text{Å}$ are due to physical gaps between the three CCDs of RSS.

explained in Srianand et al. (2008). We consider three possible locations for the dust, at z_{em} and at the redshifts of the 'red-' and 'blue-BAL' components mentioned above. We use a χ^2-minimization code to obtain the best-fitting values of two parameters, a constant normalization to match the observed flux and dust extinction in the V band (A_V) to match the spectral shape. For this fit, we consider only those regions devoid of emission or absorption lines in the spectra (see Fig. 7). We find that in all cases the fit obtained using the SMC-like extinction curve has the minimum χ^2 irrespective of the dust location. Also for a given extinction curve, dust located at z_{em} is favoured. The best-fitting values of A_V are summarized in column 9 of Table 1. The main error in A_V comes from the error in R_V. For the 1σ range in R_V found for SMC (i.e. between 2.61 and 2.87, as given in Gordon et al. 2003), the typical error in A_V is of the order of 0.01. From Table 1, it is clear that if the spectral shape is governed by dust extinction then A_V is changing between different epochs. In particular, we find a factor of ~5 increase in A_V between two SDSS epochs (i.e. epoch-1 and epoch-2) during which time we also notice that the quasar shows a *redder-when-brighter* trend.

While we have fitted the continuum using variations in A_V, it is possible that changes in the power-law spectral index also cause such a variation. To mimic this, we multiply the composite spectrum by a power law of the form $C(\frac{\lambda}{\lambda_0})^p$. Here, C, λ_0, and p are free parameters. We find the best-fitting parameters (C and p) using χ^2-minimization. The best-fitting values of p for different epochs are summarized in column 10 of Table 1 and the fits are shown in Fig. 7.

This confirms that the spectral shape changes significantly between different epochs. As expected there is a tight correlation between A_V and p.

4.2 Light curves and photometric variability

We also collected publicly available photometric light curves of J1621+0758 from the Panoramic Survey Telescope and Rapid Response System (Pan-STARRS; Chambers et al. 2016), The Palomar Transient Factory (PTF; Law et al. 2009), and the Zwicky Transient Facility (ZTF; Bellm et al. 2019a,b) surveys. PTF provides photototometric data only in the r band. Pan-STARRS provides photometric data of J1621+0758 for five broad-band filters, i.e. g, r, i, z, and y whereas ZTF gives the same for the g, r, and i bands. In both these cases, the observations in different bands were not obtained simultaneously and are typically separated by up to a few days. Photometric observations from the SDSS have also been considered.

Catalina Real-time Transient Survey (CRTS; Drake et al. 2009) provides the light curve covering nearly 11 yr (i.e. ~3.5 yr in the rest frame of J1621+0758, covering our first four spectroscopic epochs). CRTS operates without any specific filter and the resulting open magnitudes are converted to V band (corresponding to a rest wavelength of $\lambda \simeq 1750\,\text{Å}$ in the quasar frame) magnitudes using the transformation equation $V = V_{ins} + a(v) + b(v) \times (B - V)$, where V_{ins} is the observed open magnitude, $a(v)$ and $b(v)$ are the zero-point and the slope. These are obtained from three or more comparison
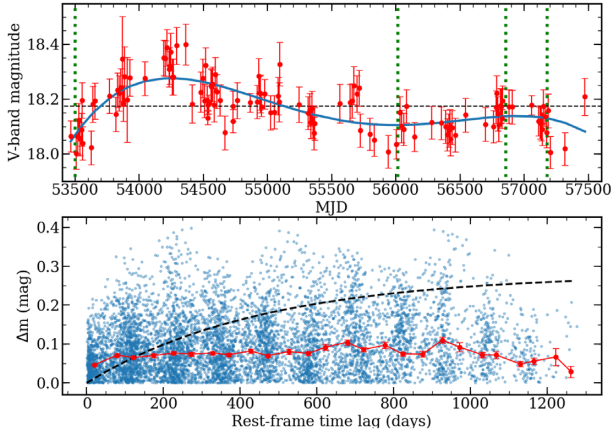
Figure 8. *Top panel:* V-band light curve of J1621+0758 from CRTS with a low-order polynomial fit overlaid. The vertical dotted lines indicate the dates of the first four spectroscopic epochs. The horizontal line gives the median V-band magnitude of J1621+0758 during this period. *Bottom panel:* Structure function obtained from the light curve shown in the top panel. The red points are the average values in a rest frame time-lag bin of 50 d. The best fit to the structure function for SDSS quasars is shown as a black dashed line (MacLeod et al. 2012). The flat structure function over 1200 d suggests that there is no fading or brightening of J1621+0758 over these time-scales.

stars in the same field with the zero-point error typically being of the order of 0.08 mag. CRTS provides four such observations taken 10 min apart on a given night. Since we are mainly interested in the long-term variability, we take the median magnitude of these four points (or less if less points are available) to get the light curves shown in Fig. 8.

Note that CRTS light curves, while sensitive to overall variations in the quasar brightness, will not capture colour variations accurately. Also these light curves will be influenced by any emission and absorption line variations. It is interesting to note that the inferred V-band magnitudes close to the two SDSS spectroscopic epochs (i.e. epoch-1 and epoch-2) are nearly identical. However, the quasar has faded by 0.3 mag (within a year in the quasar's rest frame after epoch-1) before brightening back to the first SDSS epoch value by the time epoch-2 spectrum was observed by SDSS. It is interesting to note, from the smooth polynomial fit (continuous curve in Fig. 8) to this light curve, that the V-band magnitudes are nearly same during the subsequent two spectroscopic epochs (i.e. epoch-3 and epoch-4). Just to quantify the small time-scale (i.e. <1 yr in the quasar's frame) variability we construct the structure function for the CRTS V-band magnitudes using the method described in MacLeod et al. (2012). For rest frame lag time-scale probed (i.e. up to 1200 d) the structure function is nearly flat at 0.05 mag. We do see a slight excess around a lag time of ~900 d. This basically suggests that there is no systematic brightening or fading (i.e. by more than say 0.1 mag) of J1621+0758 over the time-scales we are probing in our spectroscopic monitoring. In the bottom panel of Fig. 8, we also plot the best-fitting curve for the structure function of SDSS quasars obtained by MacLeod et al. (2012). It is clear that J1621+0758 vary much less than typical SDSS quasars over a rest frame time-scale of 200–1200 d.

The g- and r-band (corresponding to a rest wavelength of $\lambda \simeq 1530 \pm 220$ and $\lambda \simeq 1990 \pm 220$ Å, respectively) light curves of J1621+0758 constructed using photometric observations from Pan-STARRS, PTF, ZTF, and SDSS are shown in the top two panels of Fig. 9. Unlike the light curve obtained with CRTS, this combined r-band light curve sparsely samples the spell of time of the first four spectroscopic epochs. ZTF provides much better time sampling over
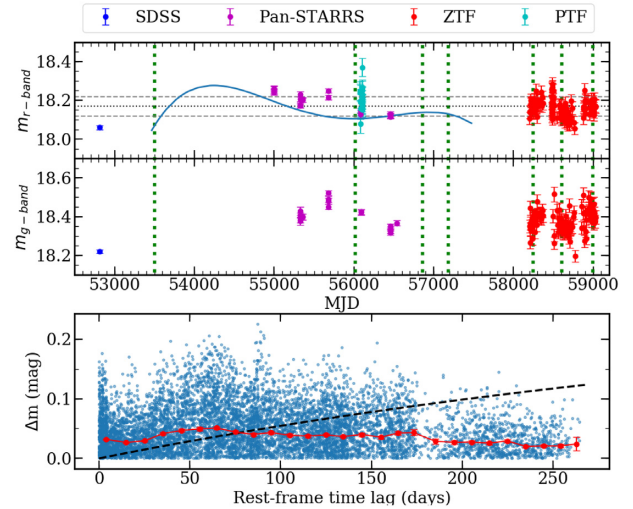

Figure 9. *Top panel:* r-band magnitudes of J1621+0758 obtained from SDSS, Pan-STARRS, ZTF, and PTF. The curve is the fit to the V-band light curve from CRTS as shown in Fig. 8. The dotted and dashed horizontal lines indicate a r-band magnitude of 18.17 ± 0.05 mag. *Middle panel:* g-band magnitudes of J1621+0758 obtained from SDSS, Pan-STARRS, and ZTF. *Bottom panel:* the structure function obtained from the r-band light curve from ZTF. There is no indication of coherent brightening or fading of J1621+0758 over time-scales of 100–250 d.

the last three spectroscopic epochs. The dotted and dashed horizontal lines show a range in r magnitude of $r = 18.17 \pm 0.05$ mag. Most of the observed points are within this range. This again confirms the lack of large coherent r-band magnitude variations over large time-scales apart from the ~0.3 mag dimming seen in the CRTS light curve (see Fig. 8 and the curve shown in Fig. 9). Also the r-band magnitudes measured close in time to the spectroscopic monitoring periods (i.e. vertical dotted lines) are nearly same. The structure function computed from ZTF r-band observations are shown in the bottom panel of Fig. 9. This also confirms that the long-term rest frame UV variability of J1621+0758 is weaker than what is found for typical SDSS quasars over a quasar rest frame time-scale of ≥ 100 d.

4.3 Colour variability

In Section 4, we used a template fitting method to derive A_V that we found to vary in the range 0.03–0.17 (see column 9 of Table 1) for the SMC extinction curve. In Fig. 10, we plot the ratio of the H I Lyman continuum flux (i.e. at $\lambda = 912$ Å) with and without reddening as a function of A_V. It can be seen that small changes in A_V can lead to large changes in the Lyman continuum flux. The reddening of the continuum can lead to a factor 3.5 reduction in the hydrogen ionizing radiation between epoch-1 and epoch-2. Similarly between epoch-2 and epoch-6, purely based on changes in A_V we expect the H I ionizing flux to increase by up to a factor 2.5. Note the SMC extinction curve is not available for the energy range above the C IV ionization level. A simple extrapolation from the UV range suggests an order of magnitude change in the C IV ionizing flux for the above-mentioned changes in A_V. Similarly if we assume a constant V-band flux, we expect a factor of 2 change in the 912 Å flux between epoch-1 and epoch-2, due to the change in the power-law index. This will correspond to a factor of ~4 change in the C IV ionizing flux. Similarly between epoch-2 and epoch-6, we expect the
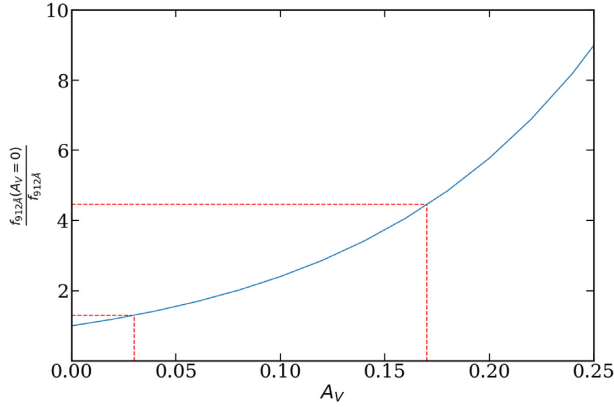
Figure 10. The ratio of the flux at 912 Å without applying any dust extinction (i.e. the dust optical depth at *V* band, $A_V = 0$) to the flux at 912 Å after applying dust extinction with A_V as given along the *X*-axis. The red dashed lines indicate the value of this ratio at $A_V = 0.03$ and 0.17 mentioned in Section 4.
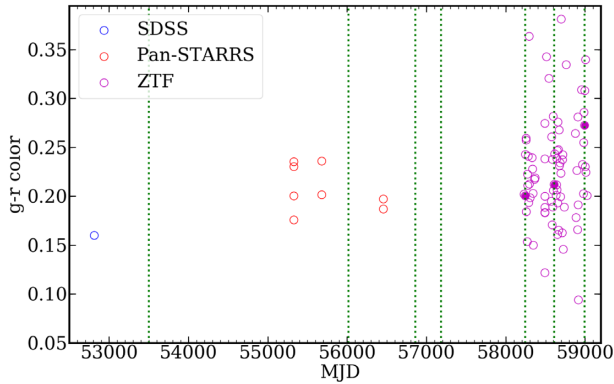

Figure 11. Plot showing $g - r$ colour as a function of time. We consider the closest *g* and *r* measurements taken within a day for this purpose. The filled symbols are the $g - r$ measurements obtained on the night of our spectroscopic observations (shown with vertical dotted lines). From the well measured ZTF colours (with a typical error of 0.04 mag), we do see large variations in the $g - r$ colours within very short time-scales.

912 Å (respectively C IV ionizing) flux to increase by a factor of ~1.6 (respectively 2.7).

Confirming the colour variations and their dependence on the quasar luminosity is important for quantifying the photoionization process. Therefore, we probe the $g - r$ colour (corresponding to the spectral shape in the rest wavelength range 1310–2310 Å) variability using available photometric observations. Remember the *g* band covers the C IV and Si IV emission lines and the C IV absorption related to both the blue- and red-BAL components. From our spectrum, we find that the net contribution of these two emission lines to the *g*-band will be ≤ 6 per cent. In Fig. 11, $g - r$ colour is shown as a function of time, where we considered only the nearest *g* and *r* band photometric points obtained within a day. It is evident that compared to SDSS photometric measurements the quasar appears to be redder in subsequent measurements. It is clear from Fig. 11 that there is no *g* $- r$ colour measurements close to the first four spectroscopic epochs. However, we do have measurements (filled circles) on the nights of the last three epochs of spectroscopic observations. We see that the $g - r$ colour varies by up to 0.3 mag (typically at $>3\sigma$ level) within a short time-scale even when the *r*-band magnitude does not vary much (see Fig. 9). It is also clear that such large colour variations
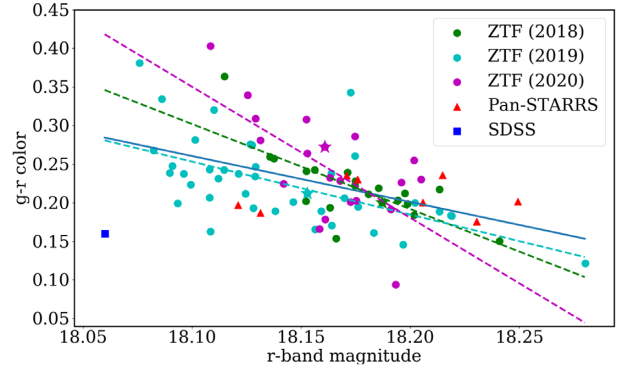

Figure 12. Plot showing the *r*-band magnitude versus $g - r$ colour using *g*- and *r*-band measurements within a day from ZTF, Pan-STARRS, and SDSS photometric surveys. The green, cyan, and magenta dashed lines correspond to linear fits of year wise (i.e. years 2018, 2019, and 2020, respectively) ZTF photometric points. The blue solid line corresponds to the linear fit to the full sample. Stars are measurements on the days when our spectroscopic observations have taken place for the last three epochs.

cannot be accounted for by the emission line variations alone (as we also see in Fig. 6).

To explore the colour variation further, we plot *r*-band magnitude versus $g - r$ colours from different observations in Fig. 12. For this, we consider only those *g*- and *r*-band photometric points that were obtained within a single night. Typical errors are <0.02 and <0.04 mag for the *r*-band magnitude and $g - r$ colours, respectively. When more observations are available on a given night in one band, we considered the nearest *g*-band measurement to the *r*-band measurement. The ZTF points obtained over the past 3 yr dominate the plot. For the full sample (without the initial SDSS point), we notice a strong anticorrelation (with spearman rank correlation coefficient of -0.45) between the two quantities in the sense that when J1621+0758 is bright in *r* band it also tends to be redder. This anticorrelation is present even when we consider data obtained each year separately. The linear regression fits to ZTF data taken during three different years are also shown by dotted lines in different colours in Fig. 12. This anticorrelation is consistent with what we see between the first two epoch spectra (see Fig. 6 and Section 4). Moreover, the $g - r$ colour has a large spread for a given *r*-band magnitude. In particular, the scatter in $g - r$ is larger for smaller *r* magnitude. This means that even if two epochs have similar *r*-band magnitudes their *g*-band magnitude (in turn the H I ionizing flux) may be very different. Simultaneous (with in a night) *r*-band and *i*-band measurements from ZTF are available only for 19 epochs (from ZTF). While $r - i$ (i.e. rest wavelength range 1720–2600 Å) colour shows 0.2 mag variation for a given *r*-band magnitude, we do not find any correlation between $r - i$ colour and *r* magnitude.

The 'redder-when-brighter' (RWB) trend shown by J1621+0758 is contrary to the general 'bluer-when-brighter' (BWB) trend shown by typical quasars during their variability (Wilhite et al. 2005; Schmidt et al. 2012; Ruan et al. 2014). Such a variability is usually attributed to global accretion rate variations or local temperature variations in a highly turbulent disc. Using multi-epoch spectroscopic data of 2169 quasars in SDSS DR7 and DR9, Guo & Gu (2016) found that 94 per cent of the quasars followed a BWB trend whereas only 6 per cent followed a red-when-brighter RWB trend. They also showed that the distributions of blackhole mass, Eddington ratio, redshift, and UV luminosity of sources showing RWB and BWB are statistically indistinguishable. Interestingly, in another study by Bian et al. (2012), almost half of the sources out of a sample of 312 radio-

loud quasars and 232 radio-quiet quasars showed RWB behaviour. It was suggested that the differences between the two samples could come from jet contribution to the continuum emission, differences in the redshift distribution of sources and time-scale probed (see section 5.5, Guo & Gu 2016).

Unlike these studies we probe the colour variations over a wide range of time-scales. In addition, our measurements from photometry are not affected by issues related to flux losses associated with variable seeing conditions. As J1621+0758 is not detected in FIRST or NVSS, we can conclude that the colour variations are not driven by the presence of a radio jet. We note that in a simple model where the flux variability is caused by local fluctuations that propagate through the accretion disc, the RWB trend can be reproduced if the fluctuations occur first in the outer accretion disc and have not yet propagated inward to the inner accretion disc region where most of the high-energy photons are created.

In summary, the light curves studied here suggest that apart from one episode between epoch-1 and epoch-2 (during which J1621+0758 experienced a continuous fading) there is no significant long term brightening or fading of the quasar over our monitoring period. The quasar shows colour variations on short time-scales suggesting possible changes in the accretion rate and/or local thermal disturbances in the disc. The RWB trend, if extrapolated to higher energy ranges that are not probed by our spectra, can lead to a significant reduction in the ionizing flux when the r-band flux increases.

5 DISCUSSIONS

5.1 C IV broad emission line variations

In the standard picture, emission line variations are usually attributed to changes in the ionizing field. In Section 3.4, we observe that the C IV emission line equivalent width varies significantly over our monitoring period. The variation is of the order of ∼11 per cent between the SDSS spectra obtained during epoch-1 and epoch-2 (∼800 d in the quasar rest frame) and ∼17 per cent between the SALT spectra of epoch-5 and epoch-7 (∼240 d in the quasar's rest frame).

Reverberation mapping studies of high-redshift, high-luminosity quasars have yielded a BLR size–luminosity relationship using the time delay between the continuum and the C IV emission line flux variations (refer to equation 2 of Kaspi et al. 2007). Using this relationship and the quasar luminosity $L_\lambda(1350\,\text{Å}) = 2.56 \times 10^{43}$ erg s^{-1} Å^{-1} measured from the epoch-1 SDSS spectrum, we estimate the C IV BLR size of J1621+0758 to be 0.10 ± 0.04 pc. Thus, we expect the response of the C IV emission line to the continuum variations to have a typical delay of up to 240 d in the quasar's rest frame (i.e. ∼750 d in the observer's frame). It is also expected that emission line variations will be diluted due to the extended nature of the BLR.

The CRTS and r-band light curves discussed in Section 4.2 show that apart from an early long-term fading there is no clear long-term variability (by more than 0.2 mag) in r-band magnitudes during our monitoring period. In particular over epoch-5, epoch-6, and epoch-7 spanning 746 d (i.e. 240 d in the quasar frame), during which we observe C IV flux variations by 17 per cent, the r-band flux has not changed by more than 0.1 mag. *Thus, it appears that the variations in the flux of ionizing photons is decoupled from that of the r-band flux. Also, the ionizing flux needs to decrease between epoch-5 and 7 in order for the C IV line flux to decrease. Alternatively the BLR in J1621+0758 is dynamically evolving without reaching a*

proper steady state equilibrium as assumed in reverberation mapping studies.

Although their numbers are increasing in the recent times, C IV reverberation mapping studies of high-z high-luminosity quasars are still rare. Lira et al. (2018) have monitored 17 targets and found that three of them show unexpected line variability (i.e. no clear correlation between r-band magnitude and emission line variabilities and/or some emission lines do not respond to continuum variations at all). In such cases, it is clear that the the r-band continuum variability do not mirror the ionizing continuum variations. Even in the well-studied NGC 5548, there are periods over which abnormal variability is noticed (Goad et al. 2016). The latter authors suggest that this abnormal variability either is due to changes in the intrinsic spectral energy distribution (SED) or is the consequence of high-energy photons obscuration by the intervening gas. This may be what happens in the case of J1621+0758.

5.2 Absorption line variability

The BAL variability is usually understood in terms of ionization changes and/or bulk motions perpendicular to our line of sight. The emergence of the blue-BAL and the emergence and subsequent disappearance of component-C of the red-BAL emphasize the importance of bulk motions in the case of J1621+0758. On the other hand, there are indications that the ionizing radiation may be changing based on the C IV emission line flux variations. Thus, it is most likely that the overall correlated variability we notice in Section 3 could be driven by both these effects. While capturing a dynamical outflow by keeping track of appropriate radiative transport is difficult (see, for example, Higginbottom et al. 2014) and beyond the scope of this work, in the following we investigate simple photoionization models and 1D disc wind models in order to interpret our results.

First, we construct photoionization models using CLOUDY v17.01 (Ferland et al. 2017) to quantify the ionization induced variations. Well-constrained photoionization modelling is possible only when several species can be discussed. The detection of Si IV and Al III absorption in the blue-BAL and Si IV during epoch-4 for the red-BAL provide this opportunity. However, due to the low-resolution spectra used here, it will be difficult to measure the column densities accurately as hidden line saturation and unknown covering factor can lead to underestimate the column densities. It is possible that the covering factors are different for different ions that will also make the observed equivalent width ratios not following the intrinsic column density ratios. Also a simple geometry considered in CLOUDY may not be a correct representation of a multiphase outflow. Given all these caveats, we use the model results as a rough guideline to infer the nature of the absorption line variability.

5.2.1 Basic CLOUDY model

We approximate the absorbing gas to be a plane-parallel slab of uniform density, n_H, having solar metallicity and illuminated from one side by the quasar radiation. The gas temperature and ionization states are computed in CLOUDY under equilibrium conditions. We consider the gas to be optically thin to H I ionization (see, for example, Hamann 1997).

First, we construct the observed wide-band SED of J1621+0758 using photometric points from the Wide-field Infrared Survey Explorer (WISE), SDSS, and Galaxy Evolution Explorer (*GALEX*) in the infrared, optical, and UV ranges, respectively (see Fig. 13). It is clear from this figure that the observed luminosities in the rest
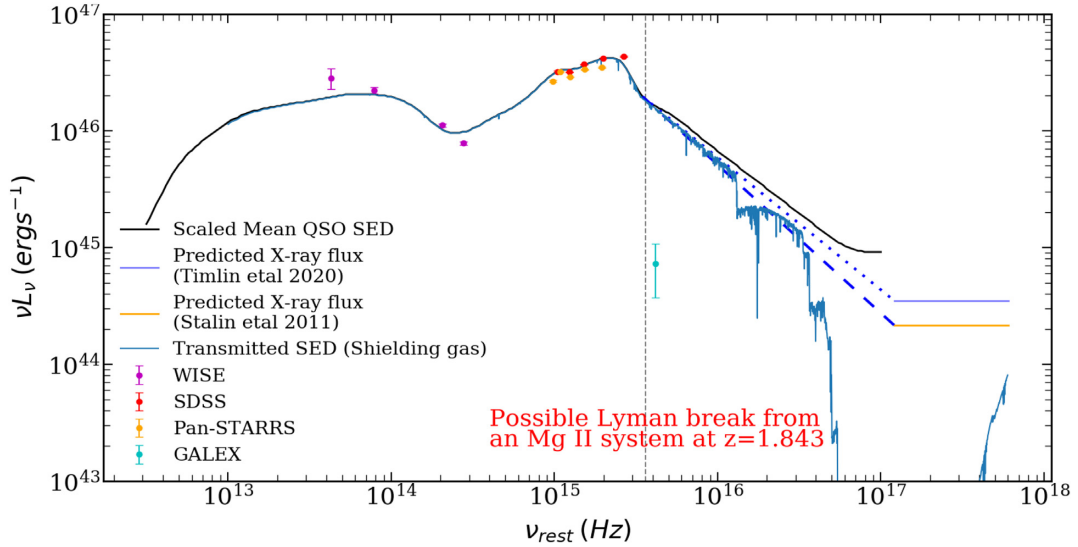
Figure 13. Broad-band spectral energy distribution of J1621+0758 created using the mean quasar SED from Richards et al. (2006) and photometric points taken from SDSS, WISE, and *GALEX*. Pan-STARRS measurements are also shown. They are slightly lower than the SDSS measurements (see Section 4.2 for variability). We extended this SED to the high energies using the observed relationship between L_{2500} and α_{OX} for non-BAL quasars (Timlin et al. 2020) and BAL quasars (Stalin, Srianand & Petitjean 2011) and these are shown with blue dotted and dashed lines, respectively. The figure also shows the non-BAL SED (i.e. blue solid line) after transmission through a shielding gaseous slab (see Section 5.2 for details). The *GALEX* measurement (cyan point) is well below our predicted SEDs. We believe this is because of Lyman continuum absorption produced by the $z = 1.843$ intervening Mg II absorber. The position of the Lyman limit of this absorber in the quasar rest frame is shown by the dashed vertical line.

frame UV-to-optical range is well reproduced by the mean non-BAL quasar SED of Richards et al. (2006). However, this predicts much higher flux in the NUV band of *GALEX* compared to what is observed (cyan point in Fig. 13). We believe this is mainly due to the H I Lyman limit of strong intervening Mg II systems found at $z_{abs} = 1.841\,82$ and $1.842\,01$ with associated absorptions from Mg I, C II, C IV, Si II, Si IV, Al II, Al III, and Fe II detected. In addition, we do see a strong Ly α absorption [with $W(\text{Ly}\,\alpha) \sim 10\,\text{Å}$] at the expected position in our NTT spectrum. However, poor SNR in this wavelength range prevents us from measuring the H I column density accurately.

As X-ray measurements are not available for J1621+0758, we have constructed the UV to X-ray part of the SED using the best-fitting relationship between α_{OX} and monochromatic luminosity at rest 2500 Å (L_{2500}) as given in Timlin et al. (2020) for a sample of 2106 radio-quiet quasars from the SDSS using Chandra observations. This gives the monochromatic luminosity at 2 KeV, $L_{2\,\text{KeV}}$. This together with the assumption that $L_\nu \propto \nu^{-1}$ in the X-ray range allows us to construct the optical to X-ray SED as shown in Fig. 13 (solid blue line). It is well known that quasars with BAL outflows tend to have lower X-ray emission compared to non-BAL quasars of similar L_{2500} (Gibson et al. 2009). In order to accommodate this, a similar procedure was carried out using the relationship between optical luminosity and α_{OX} obtained from a sample of BAL quasars as given in Stalin et al. (2011) (orange solid line in Fig. 13).

We consider a non-BAL SED modified by the presence of shielding gas or failed wind as suggested by some of the wind models (Murray et al. 1995; Proga et al. 2000) as the ionizing radiation (also shown in Fig. 13). We run CLOUDY twice to produce this SED. In the first CLOUDY run, a continuum with the modelled non-BAL SED of J1621+0758 is incident on the shielding gas with a high ionization parameter, $\log(U) = 1$ (since the shielding gas is located close to the source), total hydrogen column density $N(\text{H}) = 10^{23}\,\text{cm}^{-2}$ and solar metallicity. We obtain the transmitted continuum after it passes through the shielding gas. In the subsequent CLOUDY runs, this transmitted continuum is used as the ionizing radiation for the
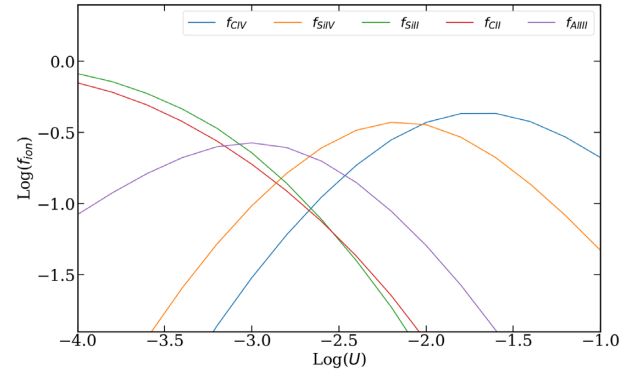

Figure 14. Ion fraction (f_{ion}) predicted by our models as a function of ionization parameter (U). The absorbing gas is assumed to be optically thin to H I ionizing photons. We have used the 'transmitted SED' shown in Fig. 13 as the ionizing radiation in our models.

absorbing gas. For the assumed SED the number of ionizing photons per second from J1621+0758 is, $Q \sim 3.4 \times 10^{56}\,\text{s}^{-1}$. In this case, the distance of the absorbing gas (r) and ionization parameter (U) are related by,

$$r = 154.6 \times \left(\frac{10^5}{n_H}\right)^{0.5} \left(\frac{10^{-1.4}}{U}\right)^{0.5}\,\text{pc}. \tag{1}$$

In Fig. 14, we show the ion fractions as a function of ionization parameter.

5.2.2 Blue-BAL absorption: ionization

Emergence of the blue-BAL was detected during epoch-2. In addition, the C IV equivalent width has initially increased and subsequently decreased after epoch-4 (see Table 2 and Fig. 1). If these changes are purely driven by ionization changes we would

like to have log $U \sim -1.5$ for epoch-4 (i.e. for which the C IV ion fraction peaks). If we assume all the ions have similar covering factor and the gas composition is of solar abundance then we will be able to infer whether log U is more or less than -1.5 during other epochs. In the epoch-2 spectrum, we detect C IV, Si IV and Al III absorption (see Fig. 2). The fact that Al III equivalent width is a factor of 2 less than that of Si IV is consistent with log $U > -2.7$ (see Fig. 14). Here, we have assumed the lines are not saturated and used the linear part of the curve of growth to estimate the column density ratios from the equivalent width ratios. Also relative abundances of metals are assumed to be that of solar values. The observed Al III optical depth is lower than that of Si IV. Therefore, in the scenario where there is partial coverage we expect the effect of saturation to be much higher for Si IV, that is why we consider the above-mentioned log U to be a lower limit. Similarly, to have C IV equivalent width twice that of Si IV we need log $U \geq -2.2$. We consider it as a lower limit as the C IV profile is much deeper than the Si IV profile.

Between epoch-2 and 3, the C IV equivalent width remained nearly the same while the Si IV equivalent width has reduced by a factor 2. This indicates an increase in the ionization parameter between epoch-2 and 3. Compared to epoch-2, the C IV equivalent width has increased by a factor of 1.5 in the spectrum taken during epoch-4. The Al III absorption is not detected in the epoch-4 spectrum with a 3σ upper limit of 0.32 Å. This trend is possible if the ionization parameter is increased between epoch-2 and 4. If the changes in n_H and r are negligible between these epochs (however see below) then increase in ionization parameter will also imply increase in the ionizing flux. Such an evolution in the ionization flux will also explain the increase in the C IV broad emission line equivalent width between these epochs. As we have seen before the C IV equivalent width starts to decrease after epoch-4. This will imply reduction in the ionization parameter. Unfortunately our spectra do not cover Si IV or Al III during the last three SALT epochs to confirm whether we detect variation in the opposite direction for Si IV and Al III absorptions. However, this will be consistent with what is required to understand the C IV emission line flux variations.

It thus seems that we have a broad coherent picture. However, if variations in the ionizing radiation is the only driver for the equivalent width variations then we would have expected the restoration of the absorption line profiles for a given equivalent width. This is not the case as can be seen from Fig. 1. Thus one has to invoke also possible kinematic shifts (i.e. acceleration) in the absorbing gas.

5.2.3 Blue-BAL absorption: kinematics

Since the blue-BAL component has emerged only during epoch-2 and shows signatures of acceleration till epoch-4, we can assume it to be located close to the accretion disc. If true, using the velocity and acceleration as a function of time we can place constraints on the exact location of the absorbing gas.

Radiatively accelerated wind models predict a radial velocity profile of the form (see Murray et al. 1995),

$$v(r) = v_\infty \left(1 - \frac{r_f}{r}\right)^\beta, \tag{2}$$

where v_∞ is the terminal velocity, $\beta \sim 1.15$ and r_f is the launching radius of the wind. Then, the acceleration profile is given by,

$$a(r) = v\frac{dv}{dr} = \beta v_\infty^2 \frac{r_f}{r^2}\left(1 - \frac{r_f}{r}\right)^{2\beta - 1}. \tag{3}$$

Once we fix r_f and v_∞ we can predict $v(t)$ and $a(t)$ for a given fluid element. We can fit the velocity and centroid shift measured at different epochs using the above two equations.

First, we consider that the absorbing gas was ejected from the place where the Keperian velocity is close to the terminal velocity. For J1621+0758, we obtain M_{BH} to be $(3.66 \pm 0.15) \times 10^9$ M$_\odot$ using the FWHM of the C IV emission (FWHM = 5977 ± 123 km s^{-1}), the monochromatic continuum luminosity, $L_\lambda(1350\,\text{Å}) = 2.56 \times 10^{43}$ erg s^{-1} Å^{-1}, measured from the first epoch SDSS spectrum (i.e. MJD of 53501) and the empirical mass–scaling relationship given by Vestergaard & Peterson (2006). We obtain $r \sim 0.4$ pc and $t \sim 11$ yr since the launching of the flow to reach the observed line-of-sight velocity in epoch-2. Using log $U \sim -1.4$ and $r = 0.4$ pc, we get $n_H \sim 1.5 \times 10^{10}$ cm^{-3} using equation (1). However, in this case we do not expect acceleration of the gas beyond epoch-2. This is inconsistent with our data. In order to accelerate the gas at latter epoch one has to perturb the steady state solution assumed here.

We therefore carefully choose the launching radius of the flow in such a way that v_{obs} and a_{obs} occurs at the same distance (r) (and hence at the same time also). In this case at $r \sim 0.040$ pc and $t \sim 1$ yr at epoch-2, this model gives epoch-2 $v_{obs} = 37\,591$ km s^{-1} and acceleration values of a few cms^{-2} which can roughly reproduce the observed changes in velocity in the subsequent epochs satisfying the observed time-scales (see Fig. 15). Also in this scenario the emergence occurs much after the first spectroscopic epoch. The consequence of the smaller launching radius are: (1) the required gas density constrained by the ionization parameter will be, $n_H \sim$ few $\times 10^{12}$ cm^{-3}; (2) the displacement of the gas between epoch-2 and 4 is ~ 0.04 pc. As this is a factor 2 change in distance from the quasar one has to take into account the change in ionization parameter from the gas motion also.

Although appealing, as pointed out by Grier et al. (2016), such models can reproduce the observed acceleration between two epochs but they cannot reproduce small jerks. While the overall velocity and acceleration evolution is captured in Fig. 15, small changes as seen between epoch-5 and epoch-7 are not reproduced. They could be due to instabilities in the flow.

5.2.4 Red-BAL absorption

As we have seen before, the largest C IV equivalent width for both A and B components was observed during epoch-4. As we do not detect any other species from component B, it is difficult to constrain model parameters. So, we focus mainly on component A. The Si IV ion fraction is maximum at log $U \sim -2.2$. If we assume solar abundance ratio for the metallicities, we need log $U \geq -2.6$ in order to produce the observed C IV to Si IV equivalent width ratio. The limit is obtained as explained in the previous section. In this case, a slow increase in the C IV equivalent width with a large increase in the Si IV equivalent width would be consistent with ionization parameter, log $U \geq -1.5$, with a decrease between epoch-2 and epoch-4. As both red- and blue-BAL components see the same radiation field, the opposite requirements for the ionization parameter is inconsistent with the simple picture of no change in n_H, r and probably total amount of gas along our line of sight [i.e. N(H)].

If the observed ejection velocity is related to the terminal velocity, then red-BAL component will be ejected at a larger r_f (i.e. ~ 6 times more) compared to the blue-BAL. Recall, components A and B emerged during epoch-2 from a broad single component seen during epoch-1. From the bottom plots of Fig. 4, we see the centroid velocity of A and B components remain nearly constant between epoch-2
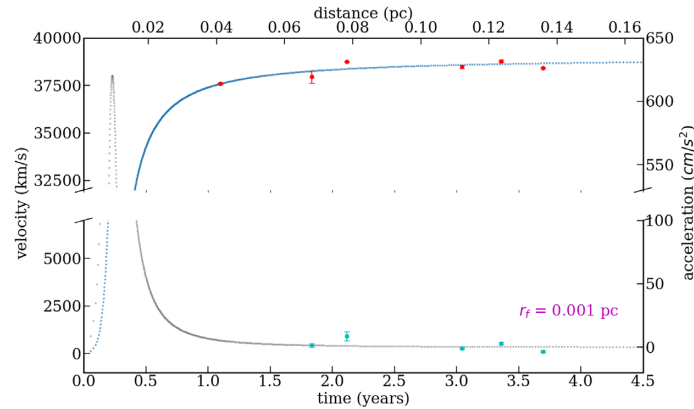
Figure 15. The velocity (blue dotted lines) and acceleration (grey dotted lines) profiles as a function of r and t are shown assuming $v_\infty = 39\,000$ km s^{-1} and $\beta \sim 1.15$.

and epoch-4. There is signature of acceleration between epoch-4 and epoch-5 before staying at constant velocity. Such a change is velocity as cannot be naturally explained by the time-steady disc wind model discussed above. One has to invoke instabilities to trigger such acceleration after a nearly constant velocity phase.

5.2.5 *Possible scenario of correlated variability*

The large outflow velocities we see for the C IV gas can originate from disc winds driven by either radiation pressure (for example Arav & Li 1994) or magnetic driving (see, for example, de Kool & Begelman 1995). In the line-driven wind models, the low ionization gas (shielded from direct heating from the central X-ray source) can be accelerated to large velocities close to the equatorial plane. Thus, the wind has a funnel-shaped structure reaching a nearly steady state with stable density and velocity profiles (Proga et al. 2000; Proga & Kallman 2004). While the disc wind models are yet to mature to the level of explaining various observed variability signatures, Dyda & Proga (2018) have shown that a time-varying radiation source can induce density and velocity perturbations in the acceleration zones of line-driven winds. It is also understood that larger the velocity of the gas, closer the gas will be to the central black hole. While it is not clear what would be the inclination of the disc wind in J1621+0758 relative to our line of sight, it is reasonable to assume that the correlated equivalent width and kinematic changes could be triggered by fluctuations in the radiation field. In particular, RWB colour variations could suggest possible propagation of fluctuations from the outer to the inner part of the disc. Measuring the column densities of different species using high resolution spectroscopy would be important to constrain the locations of red- and blue-BAL components. This is an important step to make progress in the right direction.

In the literature, various possible mechanisms are proposed to understand the kinematic shift in the absorption lines. These include directional shift of the outflow, rotation of the absorbing gas causing the line of sight velocity to change, gravitational redshift, gas infall, binary quasars, interaction with an ambient medium, etc. (Hall et al. 2002, 2013; Gabel et al. 2003; Grier et al. 2016; Joshi et al. 2019). Some of these (like interacting with ambient medium) work well to explain the deceleration seen in some BAL quasars. Mechanisms such as gas infall, binary quasars, and gravitational redshifts were introduced to understand broad absorption seen with redshifts greater than quasar redshifts. Among the above listed possibilities, the large outflow velocities and acceleration signatures seen in J1621+0758

can be explained with directional changes. Directional change can naturally occur in disc wind models where the gas trajectories are curved with respect to our line of sight probably due to magnetic field lines. With appropriate configuration, it will also be possible to explain the correlated variability as well. Such a scenario needs to be explored in simulations. On the other hand, circular trajectories can also occur if the winds are ejected from rotating discs. However, a simple rotation scenario may have issues to explain the large velocities and acceleration seen in the case of the blue-BAL and the correlated variability seen between blue- and red-BAL discussed here.

6 SUMMARY

We have presented a detailed variability analysis of BAL quasar J162122.54+075808.4 ($z_{\rm em} = 2.1395$) spectra obtained during seven epochs spanning almost 15 yr in the observer's time-scale. This has allowed us to probe the absorption and emission line variability over time-scales of $\sim$3 months to $\sim$4.8 yr in the quasar's rest frame.

J1621+0758 was identified in the SDSS survey as a BAL-QSO with C IV absorption at an ejection velocity of $v_e \sim 15\,400$ km s^{-1}, referred to as red-BAL in this work. We report the emergence of a new BAL component with associated absorption from C IV, Si IV, and Al III) with $v_e \sim 37\,500$ km s^{-1} in the second epoch spectrum, referred to as blue-BAL. We study the variability of these two BAL components using additional spectra we have obtained with NTT and SALT telescopes.

The rest equivalent width of the C IV absorption line of the blue-BAL shows an increasing trend followed by a steady decline. During the early phases the absorption profile shows kinematic shifts consistent with acceleration. The acceleration we derive between epoch-2 and epoch-3 is $+8.84 \pm 3.61$ cm s^{-2} and epoch-2 and epoch-4 is $+3.57 \pm 0.08$ cm s^{-2}. These are among the largest acceleration measured in BAL quasars (see fig. 6 of Grier et al. 2016). In the later epochs, we do see some non-monotonic centroid shifts. Such trends are not predicted by the time-steady disc wind models but often seen in BAL quasars with acceleration signatures monitored for more than two epochs.

During our monitoring period, the red-BAL shows substantial equivalent width and kinematic changes as well. The total C IV equivalent width increases in the initial stages (till epoch-4) then shows a decreasing trend consistent with what we saw for the blue-BAL component (see Fig. 4). In particular, the C IV absorption profile showed substantial variation. In the beginning, the C IV absorption profile is consistent with a single Gaussian component

(i.e. in the epoch-1 spectrum). During our monitoring period, the C IV absorption is seen in three distinct components (called A, B, and C). Component C emerged during epoch-3 and disappeared in the following epochs. The time-scale for emergence and subsequent disappearence for this component (i.e. ∼269 rest frame days in quasar's frame) is one of the shortest measured among BAL quasars. The equivalent width variations of individual components A and B follow that of the blue-BAL component. These components also show kinematic shifts consistent with acceleration between epoch-5 and 6. As in the blue-BAL, the velocity and acceleration as a function of time are inconsistent with a time-steady disc wind model predictions.

The most interesting part of the absorption line variation is the presence of correlated variability between different absorption components that are well separated in velocity space. Usually such correlated variability is associated with photoionization induced variations. To explore this, we investigate the time variability of the emission line fluxes using our spectra and of the continuum light using available photometric light curves.

The C IV emission line profile of J1621+0758 is asymmetric and consistent with the presence of outflows. We observe a clear long-term time variation of the C IV emission line equivalent width. We find that the C IV line flux varies by up to 17 per cent over the time of the observations. In the standard stratified BLR picture, this would request even larger variations in the ionizing flux. However, available optical (rest frame UV) light curves do not support any systematic brightening or fading of J1621+0758 on the corresponding time-scales. The structure function constructed from the r-band light curve is consistent with J1621+0758 being less variable compare to normal SDSS quasars. None the less, we do see $g - r$ colour variations with a 'red-when-bright' trend, the amplitude of the flux variations being larger at smaller wavelengths. Thus, if emission line variations are triggered by large ionization changes then they must be decoupled from the changes in the r-band flux. Alternatively J1621+0758 is dynamically evolving without reaching a proper steady-state equilibrium as assumed in reverberation mapping studies.

We consider simple photoionization models to gain some insights into the density of the gas and its location. Simple models with constant density and same location predict the restoration of the C IV profile for a given equivalent width. Since this is not what we observe, we rule out simple ionization changes. Disc wind models suggest that the gas density of the blue-BAL has to be larger than 10^{10} cm^{-3} to produce consistent ionization together with velocity profiles and acceleration. The observation of non-monotonic changes in the acceleration and the lack of restoration of the absorption profile can be reconciled by the presence of density and velocity fluctuations in disc winds. Simulations do suggest that a time-varying radiation source can produce such perturbations.

Therefore, in the frame work of available disc wind models, we favour density and velocity field fluctuations triggered perhaps by varying radiation field (and associated disc instabilities) to cause the observed variability in J1621+0758. Important progress could be made if we could constrain the density (and hence the location with respect to the central UV source) and the size of the absorbing gas components. For this, high-resolution spectroscopic observations of this interesting source are needed in order to derive accurate column densities and gas covering factors.

DATA AVAILABILITY

Data used in this work are obtained using SALT. Raw data will be available for public use 1.5 yr after the observing date at https://ssda.saao.ac.za/.

REFERENCES

Arav N., 1996, ApJ, 465, 617
Arav N., Li Z.-Y., 1994, ApJ, 427, 700
Bellm E. C. et al., 2019a, PASP, 131, 018002
Bellm E. C. et al., 2019b, PASP, 131, 068003
Bian W.-H., Zhang L., Green R., Hu C., 2012, ApJ, 759, 88
Buckley D. A. H., Charles P. A., Nordsieck K. H., O'Donoghue D., 2005, Proc. IAU Symp. 232, The Scientific Requirements for Extremely Large Telescopes. Cambridge University Press, Cambridge, p. 1
Burgh E. B., Nordsieck K. H., Kobulnicky H. A., Williams T. B., O'Donoghue D., Smith M. P., Percival J. W., 2003, in Iye M., Moorwood A. F. M., eds, Proc. SPIE Conf. Ser. Vol. 4841, Instrument Design and Performance for Optical/Infrared Ground-Based Telescopes. SPIE, Bellingham, p. 1463
Capellupo D. M., Hamann F., Shields J. C., Rodríguez Hidalgo P., Barlow T. A., 2011, MNRAS, 413, 908
Chambers K. C. et al., 2016, preprint (arXiv:1612.05560)
Crawford S. M. et al., 2010, in Silva D. R., Peck A. B., Soifer B. T., eds, Proc. SPIE Conf. Ser. Vol. 7737, Observatory Operations: Strategies, Processes, and Systems III. SPIE, Bellingham. p. 773725
De Cicco D., Brandt W. N., Grier C. J., Paolillo M., Filiz Ak N., Schneider D. P., Trump J. R., 2018, A&A, 616, A114
de Kool M., Begelman M. C., 1995, ApJ, 455, 448
De Rosa G. et al., 2015, ApJ, 806, 128
Drake A. J. et al., 2009, ApJ, 696, 870
Dyda S., Proga D., 2018, MNRAS, 481, 5263
Ferland G. J. et al., 2017, Rev. Mex. Astron. Astrofis., 53, 385
Filiz Ak N. et al., 2012, ApJ, 757, 114
Filiz Ak N. et al., 2013, ApJ, 777, 168
Gabel J. R. et al., 2003, ApJ, 595, 120
Gibson R. R. et al., 2009, ApJ, 692, 758
Goad M. R. et al., 2016, ApJ, 824, 11
Gordon K. D., Clayton G. C., Misselt K. A., Land olt A. U., Wolff M. J., 2003, ApJ, 594, 279
Grier C. J. et al., 2016, ApJ, 824, 130
Guo H., Gu M., 2016, ApJ, 822, 26
Hall P. B. et al., 2002, ApJS, 141, 267
Hall P. B. et al., 2013, MNRAS, 434, 222
Hamann F., 1997, ApJS, 109, 279
Hewett P. C., Wild V., 2010, MNRAS, 405, 2302
Higginbottom N., Proga D., Knigge C., Long K. S., Matthews J. H., Sim S. A., 2014, ApJ, 789, 19
Joshi R., Srianand R., Chand H., Wu X.-B., Noterdaeme P., Petitjean P., Ho L. C., 2019, ApJ, 871, 43
Kaspi S., Brandt W. N., Maoz D., Netzer H., Schneider D. P., Shemmer O., 2007, ApJ, 659, 997
Kobulnicky H. A., Nordsieck K. H., Burgh E. B., Smith M. P., Percival J. W., Williams T. B., O'Donoghue D., 2003, in Iye M., Moorwood A. F. M., eds, Proc. SPIE Conf. Ser. Vol. 4841, Instrument Design and Performance for Optical/Infrared Ground-Based Telescopes. SPIE, Bellingham, p. 1634
Kormendy J., Ho L. C., 2013, ARA&A, 51, 511
Law N. M. et al., 2009, PASP, 121, 1395

Lira P. et al., 2018, ApJ, 865, 56

McGraw S. M. et al., 2017, MNRAS, 469, 3163

MacLeod C. L. et al., 2012, ApJ, 753, 106

Murray N., Chiang J., Grossman S. A., Voit G. M., 1995, ApJ, 451, 498

Ostriker J. P., Choi E., Ciotti L., Novak G. S., Proga D., 2010, ApJ, 722, 642

Pâris I. et al., 2012, A&A, 548, A66

Proga D., Kallman T. R., 2004, ApJ, 616, 688

Proga D., Stone J. M., Kallman T. R., 2000, ApJ, 543, 686

Richards G. T. et al., 2006, ApJS, 166, 470

Richards G. T. et al., 2011, AJ, 141, 167

Rodríguez Hidalgo P., Khatri A. M., Hall P. B., Haas S., Quintero C., Khatu V., Kowash G., Murray N., 2020a, ApJ, 896, 151

Rodríguez Hidalgo P., Khatri A. M., Hall P. B., Haas S., Quintero C., Khatu V., Kowash G., Murray N., 2020b, ApJ, 896, 151

Rogerson J. A., Hall P. B., Ahmed N. S., Rodríguez Hidalgo P., Brandt W. N., Filiz Ak N., 2018, ApJ, 862, 22

Ruan J. J., Anderson S. F., Dexter J., Agol E., 2014, ApJ, 783, 105

Schmidt K. B., Rix H.-W., Shields J. C., Knecht M., Hogg D. W., Maoz D., Bovy J., 2012, ApJ, 744, 147

Srianand R., 2000, ApJ, 528, 617

Srianand R., Petitjean P., 2001, A&A, 373, 816

Srianand R., Gupta N., Petitjean P., Noterdaeme P., Saikia D. J., 2008, MNRAS, 391, L69

Stalin C. S., Srianand R., Petitjean P., 2011, MNRAS, 413, 1013

Timlin J. D., Brandt W. N., Ni Q., Luo B., Pu X., Schneider D. P., Vivek M., Yi W., 2020, MNRAS, 492, 719

Tombesi F., Cappi M., Reeves J. N., Palumbo G. G. C., Yaqoob T., Braito V., Dadina M., 2010, A&A, 521, A57

Vestergaard M., Peterson B. M., 2006, ApJ, 641, 689

Vivek M., Srianand R., Petitjean P., Mohan V., Mahabal A., Samui S., 2014, MNRAS, 440, 799

Vivek M., Srianand R., Dawson K. S., 2018, MNRAS, 481, 5570

Weymann R. J., Morris S. L., Foltz C. B., Hewett P. C., 1991, ApJ, 373, 23

Wilhite B. C., Vanden Berk D. E., Kron R. G., Schneider D. P., Pereyra N., Brunner R. J., Richards G. T., Brinkmann J. V., 2005, ApJ, 633, 638

This paper has been typeset from a TeX/LaTeX file prepared by the author.